Mon. Not. R. Astron. Soc. **353,** 529–549 (2004) doi:10.1111/j.1365-2966.2004.08090.x

Galaxy–galaxy weak lensing in the Sloan Digital Sky Survey: intrinsic alignments and shear calibration errors

Christopher M. Hirata,[1]★ Rachel Mandelbaum,[1] Uroš Seljak,[1] Jacek Guzik,[2]
Nikhil Padmanabhan,[1] Cullen Blake,[3] Jonathan Brinkmann,[4] Tamas Budávari,[5]
Andrew Connolly,[6] Istvan Csabai,[7] Ryan Scranton[6] and Alexander S. Szalay[5]
[1]*Department of Physics, Jadwin Hall, Princeton University, Princeton, NJ 08544, USA*
[2]*Astronomical Observatory, Jagiellonian University, Orla 171, 30-244 Kraków, Poland*
[3]*Princeton University Observatory, Princeton University, Princeton, NJ 08544, USA*
[4]*Apache Point Observatory, 2001 Apache Point Road, Sunspot, NM 88349-0059, USA*
[5]*Department of Physics and Astronomy, Johns Hopkins University, 3701 San Martin Drive, Baltimore, MD 21218, USA*
[6]*University of Pittsburgh, Department of Physics and Astronomy, 3941 O'Hara Street, Pittsburgh, PA 15260, USA*
[7]*Department of Physics, Eötvös University, Budapest, Pf. 32, H-1518, Hungary*

Accepted 2004 May 28. Received 2004 May 23; in original form 2004 March 19

ABSTRACT

Galaxy–galaxy lensing has emerged as a powerful probe of the dark matter haloes of galaxies, but is subject to contamination if intrinsically aligned satellites of the lens galaxy are used as part of the source sample. We present a measurement of this intrinsic shear using 200 747 lens galaxies from the Sloan Digital Sky Survey (SDSS) spectroscopic sample and a sample of satellites selected using photometric redshifts. The mean intrinsic shear at transverse separations of 30–446 h^{-1} kpc is constrained to be $-0.0062 < \Delta\gamma < +0.0066$ (99.9 per cent confidence, including identified systematics), which limits contamination of the galaxy–galaxy lensing signal to at most ∼15 per cent on these scales. We present these limits as a function of transverse separation and lens luminosity. We furthermore investigate shear calibration biases in the SDSS, which can also affect galaxy–galaxy lensing, and conclude that the shear amplitude is calibrated to better than 18 per cent. This includes noise-induced calibration biases in the ellipticity, which are small for the sample considered here, but which can be more important if low signal-to-noise ratio or poorly resolved source galaxies are used.

Key words: gravitational lensing – galaxies: haloes.

1 INTRODUCTION

Weak gravitational lensing has emerged as a powerful tool for directly measuring the matter distribution in the Universe (e.g. Bartelmann & Schneider 2001; Refregier 2003a). One of its applications has been the measurement of the projected matter density of galaxies (Brainerd, Blandford & Smail 1996; Hudson et al. 1998; Fischer et al. 2000; McKay et al. 2001; Smith et al. 2001; Guzik & Seljak 2002; Hoekstra et al. 2003; Sheldon et al. 2004; Hoekstra, Yee & Gladders 2004), groups, and clusters (Hoekstra et al. 2001, 1998; Sheldon et al. 2001). In these measurements, the observable quantity is the tangential shear γ_t of distant source galaxies induced by the lens. It is, however, possible that some of the 'source' galaxies where the shears are used to measure lensing may in fact be physically associated with the lens; in this case they may be intrinsically aligned with the lens, producing a false lensing signal. This false signal may be quantified by the 'intrinsic shear' $\Delta\gamma$, which is the spurious estimate of the tangential shear that would be obtained by applying a shear estimator to a population of physically associated galaxies (see Appendix A for a more precise definition). This intrinsic shear is essentially a type of galaxy density-shear correlation, i.e. it measures the correlation between the shears of some galaxies and the positions of others; it is distinct from the shear–shear correlations that contaminate the gravitational shear autocorrelation measured by lensing surveys in the field (Bacon, Refregier & Ellis 2000; Van Waerbeke et al. 2000; Rhodes, Refregier & Groth 2001; Hoekstra et al. 2002; Van Waerbeke et al. 2002; Brown et al. 2003; Jarvis et al. 2003).

Several people have investigated this potential contaminant of the lensing signal. Lee & Pen (2001) measured the density-shear correlation using 12 122 spiral galaxies. These authors were primarily interested in the rotation axes of galaxies and their possible use as tracers of the large-scale tidal field (and hence the cosmic density perturbations; Lee & Pen 2000) and so they measure position angles rather than shear. A crude (and model-dependent) conversion of

---

★E-mail: chirata@princeton.edu

their measurements into an intrinsic shear suggests $\Delta\gamma = -0.0037 \pm 0.0025$ at separations $r_{3D} = 500\,h^{-1}$ kpc (see Appendix B).

Bernstein & Norberg (2002) used 1819 satellite galaxies selected spectroscopically from the Two Degree Field (2dF) Galaxy Redshift Survey (Colless et al. 2001) with ellipticities measured in the Automatic Plate Measuring (APM) survey (Maddox et al. 1990) to set an upper limit on the intrinsic shear of the satellite galaxies of $|\Delta\gamma| \leqslant 0.01$ (at 95 per cent confidence)[1] for primary-satellite pairs separated by a transverse distance of $< 350\,h^{-1}$ kpc. However, this upper limit is not presented as a function of transverse separation or lens luminosity. Circularization of the galaxy images due to the APM point spread function (PSF) may weaken the upper limit slightly (by ~10–20 per cent; Bernstein & Norberg 2002) but this does not alter the conclusion that intrinsic alignment contamination of the galaxy–galaxy lensing signal observed by Fischer et al. (2000) and McKay et al. (2001) is limited to $\lesssim 20$ per cent.

There have been other observational studies of intrinsic alignments, including reported detections of higher-order density-shear statistics (Lee & Pen 2002) and shear–shear correlations (Pen, Lee & Seljak 2000; Brown et al. 2002); unfortunately there is no simple conversion from these measurements into an intrinsic shear $\Delta\gamma$.

Theoretical work on galaxy intrinsic alignments has been motivated both by inherent interest and (more recently) by contamination of cosmic shear surveys for which the intrinsic-alignment parameter of interest is the shear–shear correlation instead of the density-shear correlation. A number of estimates of the shear–shear correlations – both in *N*-body simulations and in analytical models – have been made (Croft & Metzler 2000; Heavens, Refregier & Heymans 2000; Lee & Pen 2000, 2001; Catelan, Kamionkowski & Blandford 2001; Crittenden et al. 2001; Hui & Zhang 2002; Jing 2002). Usually the galaxy is approximated as a disc aligned perpendicular to the halo angular momentum vector (for spirals) or as an ellipsoid homologous with the ellipticity of its halo (for ellipticals), although comparison to observations (Heymans et al. 2004) and simulations of galaxy formation (Van den Bosch et al. 2002) suggest that this picture is too simple and overestimates the shear–shear correlations. Of these authors, only Lee & Pen (2001) and Hui & Zhang (2002) estimate the density-shear correlation (and even then only for spirals). Using the rough conversion of Appendix B, the Lee & Pen (2001) prediction corresponds to $\Delta\gamma = -0.004$ for the spiral sources, the – sign indicating radial alignment. Hui & Zhang (2002) present some predictions for the two-dimensional (projected) density-ellipticity correlation as a function of angular separation, but do not provide a numerical estimate $\Delta\gamma(r)$.

In this paper, we use SDSS spectroscopic galaxies (as lenses) and photometric galaxies (as sources) in a luminosity-dependent study of the shear around lens galaxies due to intrinsic alignments. The large number of galaxies in the SDSS photometric sample allows tighter constraints on $\Delta\gamma$ than were obtained by Bernstein & Norberg (2002). It also provides the statistical power to compute these upper limits as a function of transverse separation and lens luminosity. To make the interpretation for weak lensing as simple as possible, we directly compute $\Delta\gamma$ using a lensing estimator (including PSF corrections) rather than the position-angle statistics of Lee & Pen (2001) or the unweighted moments computed by the APM survey.

Correct calibration of the shear estimator is necessary in order to interpret either an intrinsic alignment or a weak lensing-induced shear, particularly if the shear is detected at high signal-to-noise ratio. Errors in shear calibration can come from a variety of effects such as incomplete PSF correction, selection effects, noise-induced biases, uncertainties in PSF reconstruction, and incomplete knowledge of the ellipticity distribution of the source population (Kaiser 2000; Bernstein & Jarvis 2002; Hirata & Seljak 2003). Since we do not detect an intrinsic alignment signal, the only effect of calibration uncertainty is a minor degradation of our upper limits on $\Delta\gamma$. Nevertheless, the calibration results presented here are of direct interest for ongoing galaxy–galaxy weak lensing studies with the SDSS; calibration errors at the $\leqslant$16–18 per cent level found here are potentially important in those cases where the lensing signal is detected at $\gtrsim 6\sigma$. The noise-induced calibration biases have not been explicitly studied previously; while we find that this effect is insignificant for our sample of relatively bright ($r < 21$) galaxies, the calibration bias can be large for galaxies detected at low signal-to-noise ratio, especially if they are also not well-resolved.

This paper is organized as follows: Section 2 includes a description of the lens catalogue, and Section 3 includes discussion of the source catalogue, including details of the apparent shear measurement, the associated calibration uncertainties, and the photometric redshifts. In Section 4, we describe the methods used to compute uncertainties on the shear. Section 5 includes results for intrinsic and gravitational shear, and the results of tests for systematic errors affecting these quantities. We conclude in Section 6 with a discussion of the implications of these results. The noise-induced calibration bias derivation is presented in Appendix C.

A note concerning the cosmological model and units used in this paper: we compute the proper transverse separation of the lens and source using the physical angular diameter distance $d_A(z_l)$ to the lens. This distance is determined assuming a flat ΛCDM universe with $\Omega_m = 0.27$ and $\Omega_\Lambda = 0.73$, in accord with cosmological parameter determinations from the *Wilkinson Microwave Anisotropy Probe* (Spergel et al. 2003). We present distances in h^{-1} kpc, where h is the reduced Hubble parameter: $H_0 = 100\,h$ km s^{-1} Mpc^{-1}. When appropriately scaled by h, the angular diameter distance is only weakly sensitive even to extreme variations in cosmology: for a lens at redshift $z = 0.3$ (among the most distant in our sample; see Fig. 2 later), we find that $d_A(z_l)$ is reduced by 7 per cent if we switch from ΛCDM to an open universe ($\Omega_m = 0.27$, $\Omega_\Lambda = 0$) and by 12 per cent if we switch to an Einstein–de Sitter universe ($\Omega_m = 1$, $\Omega_\Lambda = 0$). Given that we see no detection of intrinsic alignments, the dependence of our results on Ω_m and Ω_Λ is negligible for the purpose of constraining contamination of the weak-lensing signal.

2 LENS CATALOGUE

The 'lenses' used in this investigation are obtained from the SDSS main galaxy spectroscopic sample (York et al. 2000; Strauss et al. 2002; Blanton et al. 2003a; Abazajian et al. 2004). Our sample contains 200 747 galaxies within a solid angle of 2499 deg^2 (SDSS sample 12; Blanton et al. 2003a). This sample is approximately flux-limited at Petrosian magnitude $r < 17.77$ (Strauss et al. 2002). (The r filter is centred at 622 nm; Fukugita et al. 1996). We have taken only objects at redshift $z > 0.02$; at lower redshifts, the summation

---

[1] Bernstein & Norberg (2002) reported an upper limit on the ellipticity of 0.02, which we have converted here to a shear.

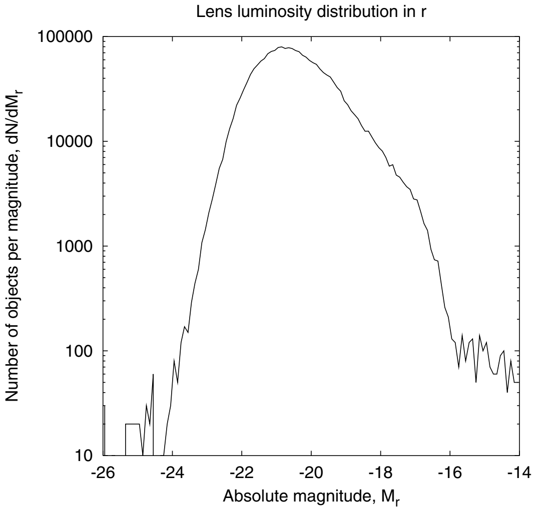

Figure 1. The magnitude distribution of lens galaxies.

of pairs of galaxies out to 1 h^{-1} Mpc transverse separation becomes computationally expensive, and little is gained anyway because of the small inverse critical surface density[2] Σ_c^{-1}. These spectra have been processed by an independent spectroscopic pipeline at Princeton (Schlegel et al., in preparation); comparisons with the survey pipeline show that the failures occur <1 per cent of the time. The objects have been extinction-corrected using the model of Schlegel, Finkbeiner & Davis (1998) extrapolated to the SDSS filters using an extinction-to-reddening ratio $R_V = 3.1$ and K-corrected to $z = 0.1$ using KCORRECT V1_11 (Blanton et al. 2003b).

Fig. 1 shows the magnitude distribution of the lens galaxies, and Fig. 2 shows their redshift distribution, overall and as a function of luminosity. We have used model magnitudes (i.e. magnitudes determined from the best-fitting de Vacouleurs or exponential profile; Stoughton et al. 2002) for both the lens and the source galaxies in this paper.

3 SOURCE CATALOGUE

3.1 Apparent shear measurement

In this section we discuss the methodology for measuring the apparent shear of source galaxies. In general, this must consist of the following steps:

(i) source galaxy detection and selection;
(ii) point spread function (PSF) determination;
(iii) measurement of galaxy ellipticity, including PSF correction;
(iv) conversion of ellipticity measurement into a shear.

If we intend to measure the radial profile of galaxy haloes, we must also use redshift and cosmological information to convert the shear measurements into constraints on the mass distribution. However, in this paper we are only interested in determining the spurious contribution to the apparent shear from intrinsic alignment of source and lens galaxies. Therefore, we only work through the four steps outlined above. Also, the reconstruction of the PSF from stellar images is carried out by standard SDSS software (Stoughton et al. 2002, Lupton et al., in preparation) and will not be described here.

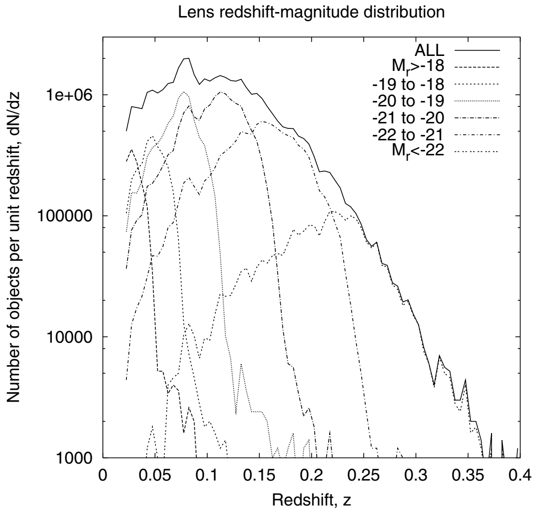

Figure 2. The redshift distribution of lens galaxies, overall and as a function of luminosity. Note that the brighter (smaller M_r) subsamples peak at higher redshift.

3.1.1 Adaptive moments

We begin by defining the adaptive moments, which are used in the source selection and ellipticity measurement. The adaptive second moment matrix M of the image intensity $I(x, y)$ of a galaxy is found by minimizing the energy functional:

$$E(A, x_0, y_0, \mathsf{M}; I) = \frac{1}{2}\int \left|I(x, y) - A\mathrm{e}^{-\rho^2/2}\right|^2 \mathrm{d}x\,\mathrm{d}y, \qquad (1)$$

where

$$\rho^2 = (\boldsymbol{r} - \boldsymbol{r}_0)^T \mathsf{M}^{-1} (\boldsymbol{r} - \boldsymbol{r}_0) \qquad (2)$$

and $\boldsymbol{r} = (x, y)$. The vector $\boldsymbol{r}_0$ is the object centroid, and the moment matrix M is taken to be symmetric and can be parametrized as

$$\mathsf{M} = \frac{T}{2}\begin{pmatrix} 1 + e_+ & e_\times \\ e_\times & 1 - e_+ \end{pmatrix}, \qquad (3)$$

where T is called the trace, and $\mathbf{e} = (e_+, e_\times)$ form the spin-2 ellipticity. As defined here the ellipticity is restricted to lie in the unit circle $e_+^2 + e_\times^2 \leqslant 1$.[3] The trace is one measure of the 'size' of an object; another is the geometric mean σ of the semi-major and semi-minor axes:

$$\sigma^2 = \frac{T}{2}\sqrt{1 - e^2} = \sqrt{\det \mathsf{M}}, \qquad (4)$$

where $e^2 \equiv e_+^2 + e_\times^2$. The energy functional is minimized by requiring:

$$\mathsf{M} = 2\frac{\int (\boldsymbol{r} - \boldsymbol{r}_0)(\boldsymbol{r} - \boldsymbol{r}_0)^T I(x, y)\mathrm{e}^{-\rho^2/2}\,\mathrm{d}x\,\mathrm{d}y}{\int I(x, y)\mathrm{e}^{-\rho^2/2}\,\mathrm{d}x\,\mathrm{d}y}; \qquad (5)$$

---

[2] The inverse critical surface density is defined by $\Sigma_c^{-1} = 4\pi G D_{\mathrm{OL}} D_{\mathrm{LS}}/c^2 D_{\mathrm{OS}}$, where D_{OL}, D_{LS} and D_{OS} are the angular diameter distances from the observer to the lens, the lens to the source, and the observer to the source. This quantity is useful because it packages the geometrical aspects of lensing together; the shear signal for a given weak lens at fixed physical transverse separation r scales $\gamma \propto \Sigma_c^{-1}$.

[3] We warn the reader that the definition of ellipticity is not standard across the literature. This definition is consistent with Bernstein & Jarvis (2002), but not with Kaiser, Squires & Broadhurst (1995).

if the centroid were also determined adaptively, we would simultaneously solve

$$0 = \int (\boldsymbol{r} - \boldsymbol{r}_0) I(x, y) \mathrm{e}^{-\rho^2/2}\, \mathrm{d}x\, \mathrm{d}y. \tag{6}$$

However, the SDSS photometric pipeline (PHOTO) fixes $\boldsymbol{r}_0$ at the centroid of the object finder rather than iteratively solving equation (6). We also use the radial fourth moment a_4 defined by:

$$2(1 + a_4) = \frac{\int \rho^4 I(x, y) \mathrm{e}^{-\rho^2/2}\, \mathrm{d}x\, \mathrm{d}y}{\int I(x, y) \mathrm{e}^{-\rho^2/2}\, \mathrm{d}x\, \mathrm{d}y}. \tag{7}$$

PHOTO computes the adaptive moments $\mathbf{M}$ and a_4 for both the observed (i.e. not deconvolved) galaxy image $I(x, y)$ and the reconstructed PSF $P(x, y)$. We will denote moments corresponding to the galaxy image with a superscript (I) and those corresponding to the PSF with a superscript (P). The (raw) resolution factor R_2 is defined by:

$$R_2 = 1 - \frac{T^{(P)}}{T^{(I)}}; \tag{8}$$

in the limit of a very well-resolved galaxy, $R_2 \to 1$, whereas for a poorly resolved galaxy the observed image is very similar to the PSF ($I \approx P$) and so $R_2 \to 0$.

The physical interpretation of $\mathbf{M}^{(I)}$ is as a best-fitting Gaussian to the image profile. The fourth moment $a_4^{(I)}$ parametrizes the departure of the galaxy from Gaussianity: it is 0 for a Gaussian profile, 0.17 for an exponential profile, and 0.40 for a de Vacouleurs profile. The fourth moment of the PSF diagnoses the deviation of the PSF from Gaussianity. In particular, a PSF dominated by Kolmogorov turbulence [optical transfer function $\propto \mathrm{e}^{-(l/l_0)^{5/3}}$; Kaiser 2000] should have $a_4^{(P)} \approx 0.046$, in good agreement with the typical PSF in the SDSS.

3.1.2 *Source galaxy selection*

Our source galaxies are selected from the SDSS photometric catalogue (York et al. 2000; Hogg et al. 2001; Smith et al. 2002; Stoughton et al. 2002; Abazajian et al. 2003; Pier et al. 2003). The catalogue is based on images from the SDSS camera (Gunn et al. 1998) processed at Princeton by the PHOTO software (Lupton et al. 2001, in preparation; Finkbeiner et al. 2004). In order to avoid the PSF anisotropy-induced selection bias discussed by Kaiser (2000) and Bernstein & Jarvis (2002), PHOTO applies a convolution to each image to circularize the effective PSF before running the object detection algorithm. We only consider objects that are classified by PHOTO as galaxies, are not deblended, do not contain saturated pixels, and do not have flags set indicating possible problems with the measurement of the image. We reject objects where the adaptive moment measurements failed, the resolution factor $R_2 < \frac{1}{3}$, the measured ellipticity $e_+^{(I)2} + e_\times^{(I)2} > 0.95$, or the radial fourth-moments $|a_4^{(I)}| > 0.99$ or $|a_4^{(P)}| > 0.99$ in at least two of the *g*, *r* and *i* bands. Objects with extinction-corrected model magnitude fainter than 21 in *r*-band or with failed photometric redshifts (see Section 3.3) are also rejected. In case of multiple observations of the same object, we take the observation where the *i*-band resolution factor is largest.

Our final source galaxy catalogue contains $N_s = 6\,975\,528$ galaxies, although some of these are in regions of the SDSS without spectroscopic coverage and hence are not actually used in the analysis.

3.1.3 *Measurement of galaxy ellipticities*

Since most galaxies used in weak lensing measurements are of comparable angular size to the PSF, the ellipticity $[e_+^{(I)}, e_\times^{(I)}]$ determined from the galaxy image $I(x, y)$ is generally not equal to the true ellipticity of the galaxy. Therefore, a correction for the PSF is necessary. The basic idea of any such correction is to treat the observed galaxy image I as a convolution of the PSF P and a pre-seeing image f:

$$I(x, y) = \int f(x', y') P(x - x', y - y')\, \mathrm{d}x'\, \mathrm{d}y'. \tag{9}$$

The problem is to determine the ellipticity of the pre-seeing image f from I and P. This problem has been considered by many authors (Kaiser et al. 1995; Luppino & Kaiser 1997; Kaiser 2000; Bernstein & Jarvis 2002; Hirata & Seljak 2003; Refregier & Bacon 2003); we use the 'linear' method of Hirata & Seljak (2003) because it can be implemented using the PHOTO outputs.

The 'linear' method is based on the observation that if the galaxy and PSF are Gaussian, then the adaptive second moment matrix of I is related to that of the PSF and the pre-seeing image by:

$$\mathbf{M}^{(I)} = \mathbf{M}^{(f)} + \mathbf{M}^{(P)}, \tag{10}$$

implying:

$$\mathbf{e}^{(f)} = \frac{\mathbf{e}^{(I)}}{R_2} + \left(R_2^{-1} - 1\right)\mathbf{e}^{(P)}. \tag{11}$$

Hirata & Seljak (2003) made the approximation that the pre-seeing galaxy image and the PSF can be approximated by the quartic-Gaussian form:

$$f(x, y) \propto \left[1 + \frac{a_4}{2}(\rho^4 - 4\rho^2 + 2)\right] \mathrm{e}^{-\rho^2/2}, \tag{12}$$

where ρ is given by equation (2) and similarly for $P(x, y)$. Within this approximation, we can compute the corrections to equation (10) to first order in $a_4^{(I)}$ and $a_4^{(P)}$. The calculation is straightforward (although tedious) and is given in Appendix B of Hirata & Seljak (2003); it results in a correction to the resolution factor R_2. We compute ellipticity estimators $[\hat{e}_+^{(f)}, \hat{e}_\times^{(f)}]$ using the formulae presented there. Measurement errors on $\mathbf{M}^{(I)}$ are computed by PHOTO from the Fisher matrix, and propagated into errors on $\mathbf{e}^{(f)}$ via numerical differentiation of the PSF correction formulae.

The actual image of the galaxy and the reconstructed PSF are both pixelized, and in principle, the PSF correction should take this into account. Mathematically, pixelization is a two-step process consisting of convolution with a square top-hat function (i.e. integration over the pixel area), followed by sampling at the centre of each pixel. So long as the convolution step is applied to both the PSF and the galaxy, it does not cause concern for us because equation (9) is still valid. The sampling at the centre of each pixel replaces the integration in the moment computation with summation over pixels, which causes a problem for the integrals in equation (5) if the integrand is insufficiently sampled (i.e. if there is a high-wavenumber component aliased to zero wavenumber); this occurs for wavenumbers:

$$l \geqslant l_{\text{alias}} = \frac{2\pi}{\theta_{\text{pixel}}} \approx 3.28 \times 10^6 \approx 15.9\ \text{arcsec}^{-1}. \tag{13}$$

Aliasing is more likely to occur for the PSF measurement than the galaxy measurement as the PSF is smaller in real space. If the PSF were a Gaussian with $\theta_{\text{FWHM}} = 1.2$ arcsec (better than typical seeing in the SDSS), the function $P(\boldsymbol{r})\mathrm{e}^{-\rho^2/2}$ [where ρ^2 is determined from equation (2) using $\mathbf{M}^{(P)}$] has 1σ width of 0.36 arcsec in real space and 2.8 arcsec^{-1} in Fourier-space. Therefore, we do not expect a significant contribution to the moment integrals at the aliasing wavenumber $l_{\rm alias}$, and we have not applied any correction for pixelization.

We have determined the camera shear via differentiation of the SDSS astrometric solution (Pier et al. 2003), and found it to be < 0.2 per cent in all three bands (g, r, i) used for the ellipticity measurement in all six camera columns. Given that the camera shear is small and is not correlated with the locations of lens galaxies, no correction for camera shear has been applied. Our search for a shear signal around random points (Section 5.2) produced a null result, confirming that camera shear contamination of the intrinsic alignment signal is negligible.

The ellipticities $\mathbf{e}^{(f)}$ are measured separately in the g, r and i bands (the u and z bands typically have lower signal-to-noise ratio and so are not as useful for ellipticity measurement). An overall ellipticity is computed for each source galaxy by performing an average (weighted by the measurement error) of the ellipticities in the bands in which ellipticity measurement was successful. At this stage we reject objects with ellipticities $e^{(f)2} > 2$.

3.1.4 Ellipticity to shear conversion

Once the ellipticities of the source galaxies have been determined, it is necessary to convert them into a shear estimator. The simplest such estimator is obtained by dividing the ellipticity by an appropriate 'shear responsivity factor' $\mathcal{R}$:

$$\hat{\gamma} = \frac{\sum_{j=1}^{N_s} \hat{\mathbf{e}}_j}{\mathcal{R} N_s}, \tag{14}$$

where N_s is the number of source galaxies measured. Here $\mathcal{R}$ measures the response of the mean ellipticity to an applied shear, $\langle \hat{\mathbf{e}} \rangle = \mathcal{R}\gamma + O(\gamma^2)$. It is given by:

$$\mathcal{R} = 2\left(1 - e_{\rm rms}^2\right) \tag{15}$$

(Bernstein & Jarvis 2002), where $e_{\rm rms}$ is the rms ellipticity per component (+ or ×). From Fig. 3, we find $e_{\rm rms} \approx 0.37$. (The factor of 2 comes from the fact that a shear of 1 per cent, when applied to a circular object, yields an ellipticity of 2 per cent.)

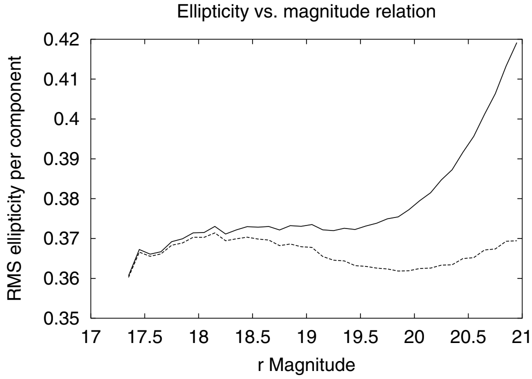

Figure 3. The measured rms ellipticity of our galaxies per component (i.e. not the total rms ellipticity, which is $\sqrt{2}$ times greater as ellipticity has two components) as a function of r magnitude. The solid curve is the rms of the measured ellipticities, while for the dashed curve the measurement noise has been subtracted out. For brighter galaxies, the rms ellipticity per component is 0.37, which is the value we use to compute the shear responsivity. (The statistical significance of the downward dip at $r \approx 20$ is large, but its amplitude is only 3 per cent, which makes it smaller than possible calibration errors. It is therefore possible that this does not represent a real feature in the galaxy ellipticity-magnitude distribution.)

In principle, better shear signal-to-noise ratio can be obtained if galaxies are weighted according to the ellipticity measurement error (Fischer & Tyson 1997; McKay et al. 2001) or if an ellipticity-dependent weight is used (Hoekstra, Franx & Kuijken 2000; Kaiser 2000; Bernstein & Jarvis 2002). Since we only use bright ($r < 21$) galaxies, for which the measurement error is subdominant to the shape noise, weighting by measurement error is not helpful. Also, while ellipticity-dependent weighting is useful for measurement of gravitational shear, it complicates the interpretation of intrinsic alignment studies as the apparent shear from intrinsic alignments probably depends at some level on the method of weighting. Therefore, in this paper we use only the 'unweighted' estimator, equation (14).

Because there is insufficient signal-to-noise ratio for a shear measurement around one galaxy, we report the shear measurement averaged in annular bins around many lens galaxies. We compute the galaxy-apparent shear correlation function $\gamma_t(r)$ averaged in the annular bin $r_- < r < r_+$ by pair summation,

$$\gamma_t(r_-, r_+) = \frac{\sum_{\alpha,j} \gamma_{t,\alpha j}}{N_p(r_-, r_+)}, \tag{16}$$

where the summation is over lenses α and sources j; $N_p(r_-, r_+)$ is the number of lens–source pairs with separations between r_- and r_+; and $\gamma_{t,\alpha j}$ is the + component of the apparent shear of source j in coordinates where the x-axis is aligned perpendicular to the line connecting the lens and source, and the y-axis is aligned along the line connecting the lens and source. That is, γ_t is the 'tangential' shear component (so that lensing-induced shears are positive). In addition to γ_t, we report the shear γ_{45} at a 45° angle to the lens (the × component in the coordinate system aligned with the lens–source direction). The latter must vanish in the mean by symmetry, but is nevertheless useful for confirmation of the uncertainty estimates.

3.2 Calibration uncertainty

In order to interpret the results of either intrinsic or gravitational lensing shear measurements, we must understand two types of systematic errors in the shear measurements: additive biases, which are independent of the shear signal; and multiplicative or calibration biases, which affect the response of the shear estimator to an actual shear. Additive biases (due to PSF ellipticity, for example) constitute a source of spurious power in the shear power spectrum and hence are a serious issue for cosmic shear surveys that aim to measure this power spectrum. However, as we are essentially computing a cross-correlation function between the galaxy density and shear, the additive bias can be determined by repeating the galaxy-shear correlation function measurement using a random 'lens' galaxy catalogue (see Section 5.2). Computing the calibration bias is much harder as there is no straightforward way to measure it directly. At present, then, the calibration bias must be understood theoretically by considering all known sources of calibration error. The major sources of error are shown in Table 1 along with their estimated uncertainty. Note that these systematic error estimates are in some cases very rudimentary and should be considered only as rough guides to the level at which systematics might be affecting our results.

In addition to the sources of error mentioned in the table, there are two other phenomena in weak lensing surveys that can mimic a calibration error: source redshift errors and stellar contamination. An error in the source redshift distribution results in incorrect determination of the lensing strength Σ_c^{-1} and hence the surface density contrast $\Delta\Sigma$; however, as our objective here is to measure apparent shear rather than mass, this effect is not relevant to the intrinsic

Table 1. Identified sources of calibration error $\delta\gamma/\gamma$ in the apparent shear measurement, and rough upper limits to the level of error they might induce. (see the text for caveats.)

Source	Calibration error (per cent)
PSF dilution correction	-8 to $+6$
PSF reconstruction	$\pm$ 1.9
Shear selection bias	$\pm$ 5.0
Shear responsivity error	$\pm$ 1.7
Noise-rectification bias	-1.1 to $+1.4$
Total	-18 to $+16$

alignment estimation. Stellar contamination of the ‘source galaxy’ sample can dilute the shear signal, resulting in an effective calibration bias in galaxy–galaxy lensing, however, this does not affect our measured intrinsic shear signal because we divide our intrinsic shear signal by the fraction of our sources that are physically associated with the lens (as determined by the lens–source correlation function or ‘pair ratio’; see Section 5). Stars are not clustered around the lens galaxies and so their dilution effect on the observed shear and the physically associated fraction cancel out in the estimate of $\Delta\gamma$.

In the remainder of this section we discuss each of the biases in Table 1. In each case, our aim is to estimate or constrain the induced calibration bias $\delta\gamma/\gamma$, defined by:

$$\frac{\delta\gamma}{\gamma} \equiv \frac{1}{2}\left(\frac{\partial\langle\hat{\gamma}_+\rangle}{\partial\gamma_+} + \frac{\partial\langle\hat{\gamma}_\times\rangle}{\partial\gamma_\times}\right)\bigg|_{\gamma=0} - 1, \qquad (17)$$

where $\langle\hat{\gamma}\rangle$ is the expectation value of the shear estimator. Note that $\delta\gamma/\gamma = 0$ for an unbiased shear estimator ($\langle\hat{\gamma}\rangle = \gamma$). If $\delta\gamma/\gamma$ is positive, then any galaxy-shear correlation signal will be overestimated; if $\delta\gamma/\gamma$ is negative, the signal will be underestimated. In principle, $\delta\gamma/\gamma$ may vary with angular position, however, in computing the effective calibration bias for the galaxy-shear correlation we only care about the average value of $\delta\gamma/\gamma$.

3.2.1 PSF dilution correction

As noted in Section 3.1.3 we do not measure the galaxy ellipticity $\mathbf{e}^{(f)}$ directly but rather the measured image ellipticity $\mathbf{e}^{(I)}$, which has been diluted by the blurring effect of the PSF. Our correction for this effect is not perfect as the quartic-Gaussian form (equation 12) is not a perfect model for the ellipticity of the galaxy or PSF, and this can lead to a calibration error.

The calibration error in the PSF dilution correction for adaptive moment methods was studied in detail in Hirata & Seljak (2003) (an analysis for the non-adaptive moment methods can be found in Erben et al. 2001). Hirata & Seljak (2003) found that for the range of parameters of interest here, the ‘linear’ correction can have calibration bias between -8 and $+13$ per cent (the worst case being exponential-profile galaxies where the resolution factor is near our limit $R_2 \approx \frac{1}{3}$). However, we note that for 81 per cent of our source galaxies, $R_2 \geqslant \frac{1}{2}$, and within this range Hirata & Seljak (2003) found that $\delta\gamma/\gamma$ ranges from -8 to $+4$ per cent. Using this tighter constraint for the $R_2 \geqslant \frac{1}{2}$ galaxies, and the -8 to $+13$ per cent range for the 19 per cent of our sample with $\frac{1}{3} \leqslant R_2 \leqslant \frac{1}{2}$, we constrain $\delta\gamma/\gamma$ for the overall sample to lie in the range of -8 to $+6$ per cent. This is the range of values shown in Table 1.

It can be seen from Table 1 that the PSF dilution correction is currently the largest item in the calibration error budget; this error will be reduced in future studies by using more accurate but computationally expensive PSF correction methods such as re-Gaussianization (Hirata & Seljak 2003) or shapelet decomposition (Refreiger 2003b; Refregier & Bacon 2003).

3.2.2 PSF reconstruction

The SDSS PSF is reconstructed using images of the bright stars by the PSP pipeline (Stoughton et al. 2002). Any error in the PSF model used in the PSF correction can translate into an error in the ‘PSF-corrected’ ellipticity $\mathbf{e}^{(f)}$. Two major types of error concern us here: ellipticity errors and trace (size) errors. Ellipticity errors introduce spurious power into the shear measurements, which can be a serious problem for shear autocorrelation measurements (Jarvis et al. 2003; Hoekstra 2004); however, to lowest order these are less serious for galaxy–galaxy lensing because these errors are not expected to correlate with the locations of galaxies. If the size $T^{(P)}$ of the PSF is systematically over or underestimated, this leads, respectively, to under or overestimation of the ellipticity $\mathbf{e}^{(f)}$, and hence to a shear calibration error. We have tested the PSF traces by comparing them to the observed traces $T^{(I)}$ of ‘stars’ (as identified by PHOTO) with PSF magnitude uncertainty[4] in the range 0.05–0.1 (1σ). Fainter stars are not used because their moments are too noisy; brighter stars are not used because they have been used as part of the PSF fitting and hence the errors in their moments may not be representative of the typical error in PSF reconstruction.

An estimate of the systematic error in the PSF trace can be obtained by considering the quantity $q = \ln[T^{(I)}/T^{(P)}]$. If the PSF reconstruction were perfect, we would have [to second order in $\delta T^{(I)} = T^{(I)} - T^{(P)}$]:

$$\langle q\rangle = \frac{\left\langle \delta T^{(I)}\right\rangle}{T^{(P)}} - \frac{1}{2}\frac{\left\langle \delta T^{(I)2}\right\rangle}{T^{(P)2}} = \frac{2}{\nu^2}, \qquad (18)$$

where ν is the signal-to-noise ratio, and we have used equation (C26) for the bias and variance of the adaptive trace estimator, assuming the ellipticity of the PSF is small compared with unity. The signal-to-noise ratio, for near-Gaussian PSF, is related to the PSF magnitude uncertainty σ_{PSFmag} via $\nu = 0.4\ \ln\ 10/\sigma_{\mathrm{PSFmag}}$. Thus the log trace ratio q has expectation value

$$\langle q\rangle = 0.0236\left(\frac{\sigma_{\mathrm{PSFmag}}}{0.1}\right)^2 + O\left(\sigma^3_{\mathrm{PSFmag}}\right), \qquad (19)$$

which varies from 0.0059 to 0.0236 over the range of signal-to-noise ratios considered.

The tail-rejected means obtained from the stars are $\langle q\rangle = -0.0087$, -0.0086 and -0.0086, in g, r and i, respectively, if objects more than 3σ from the mean are rejected; and $+0.0057$, $+0.0057$ and $+0.0056$ (with rejection at 7σ). Comparison of these numbers to equation (19) suggest that the systematic bias in $q = \ln[T^{(I)}/T^{(P)}]$ induced by PSF reconstruction errors is $\leqslant 3$ per cent, i.e. that if $T^{(P)}$ is being systematically over or underestimated by PSP then the magnitude of this effect is no more than 3 per cent. We have therefore computed the systematic error in Table 1 assuming $\delta T^{(P)}/T^{(P)} = \pm\ 0.03$. The conversion to a shear calibration is obtained by differentiation of equation (11) with respect to $T^{(P)}$, neglecting the non-Gaussian correction to R_2. This yields, to first

---

[4] The PSF magnitude of an object is computed by fitting a PSF to the image of the object and finding the best-fitting normalization.

order,

$$\frac{\delta\gamma}{\gamma} = \frac{\delta e_+^{(f)}}{e_+^{(f)}} = -\frac{\delta R_2}{R_2} = \left(R_2^{-1} - 1\right)\frac{\delta T^{(P)}}{T^{(P)}} \tag{20}$$

(the error for $e_\times$ is the same). The mean value of $R_2^{-1} - 1$ for our sample of galaxies is 0.62; multiplying by 0.03 gives the systematic error estimate in Table 1.

3.2.3 *Shear selection bias*

If the algorithm for selecting galaxies preferentially selects galaxies that are nearly circular, then the estimated shear (as computed from equation 14) will be closer to zero than the true shear. This could arise, e.g. because after PSF convolution a circular galaxy is spread over fewer pixels (and hence will be detected at higher signal-to-noise ratio) than a highly elongated galaxy with the same magnitude and pre-seeing area. The actual selection algorithm used here is more sophisticated than a simple signal-to-noise ratio cut; we expect that some of our cuts, e.g. the magnitude cut at $r < 21$, will be relatively insensitive to shear selection biases, whereas others, e.g. the resolution factor cut at $R_2 \geqslant \frac{1}{3}$, will not. In principle, the shear selection bias would be eliminated if the selection algorithm consisted of a simple cut on the magnitude of the galaxy (which is shear-independent), however, in practice one needs additional cuts, e.g. to remove unresolved galaxies from the catalogue.

The shear selection bias is difficult to compute from first principles because of cuts made on the galaxy sample (convergence of adaptive moments, flags, resolution factor cut, ellipticity cut, magnitude cut, etc.). Of these, the most worrying are the resolution factor cut and the adaptive moment convergence. In general, the shear selection bias is given by (Hirata & Seljak 2003):

$$\frac{\delta\gamma_+}{\gamma_+} = \frac{1}{\mathcal{R}}\left\langle e_+^{(f)} \frac{\partial}{\partial\gamma_+} \ln\mathcal{P}\right\rangle, \tag{21}$$

where the average is taken over galaxies used for the measurement; $\mathcal{P}$ is the probability of a galaxy being detected and selected; e is the ellipticity of the galaxy; and γ is the gravitational shear (a similar equation holds for $\delta\gamma_\times$). Conceptually, this equation is telling us that if the selection probability is decreased by applying an infinitesimal shear that makes the galaxy more elliptical, then the shear will be underestimated.

Given the absence of a good theoretical model of selection biases, we parametrize the problem by assuming that there is a selection probability that is a function of the ellipticity, $\mathcal{P}(e)$, and that we may approximate $\ln\mathcal{P}(e)$ using a polynomial of the order of 2α:

$$\ln\mathcal{P}(e) = \sum_{j=0}^{\alpha} c_{2j} e^{2j} \tag{22}$$

(odd-order terms in e are forbidden by symmetry). The distribution of galaxy ellipticities is shown in Fig. 4(a). In Fig. 4(b), we have added noise to the ellipticities so that all the galaxies have the same ellipticity noise $\sigma_e = 0.25$ (i.e. we have added random increments Δe_+ and $\Delta e_\times$ of variance $\sqrt{0.25^2 - \sigma_e^2}$ to each component of the ellipticity). If we assume that the difference between the $r < 19.0$ and $20.5 < r < 21.0$ curves in Fig. 4(b) is entirely due to selection biases, then we should have:

$$\ln\frac{n_{20.5<r<21.0}(e)}{n_{r<19.0}(e)} = \sum_{j=0}^{\alpha} c_{2j} e^{2j} + \text{constant}. \tag{23}$$

A fit to this equation in the range $0 < e < 1.5$ using $\alpha = 4$ (five parameters) gives $c_2 = -0.0178$, $c_4 = -0.281$, $c_6 = +1.140$ and $c_8 = +0.205$. (We fit beyond the maximum $e = 1.414$ used in this paper to suppress the characteristic 'ringing' of polynomial fits.) Substituting this fit into equation (21) and noting that $\mathrm{d}e/\mathrm{d}\gamma_+ = 2e_+(1 - e^2)$, we find that the shear selection bias is:

$$\begin{aligned}\frac{\delta\gamma}{\gamma} &= \frac{1}{\mathcal{R}}\int e(1 - e^2)n(e)\frac{\mathrm{d}\ln\mathcal{P}}{\mathrm{d}e}\,\mathrm{d}e \\ &= \frac{1}{\mathcal{R}}\int_0^{e_{\max}} (1 - e^2)n(e)\left(\sum_{j=1}^{\alpha} 2jc_{2j}e^{2j}\right)\mathrm{d}e. \end{aligned}\tag{24}$$

(a) Ellipticity distribution (measured)

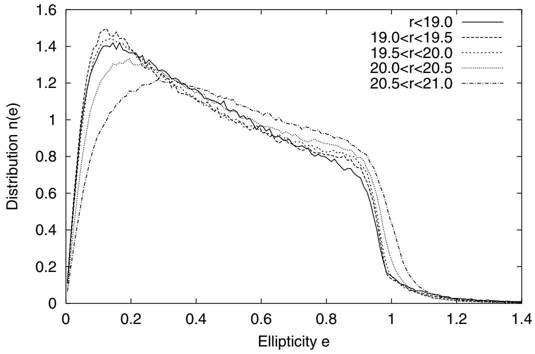

(b) Ellipticity distribution (with added noise, σ_e^{tot}=0.25)

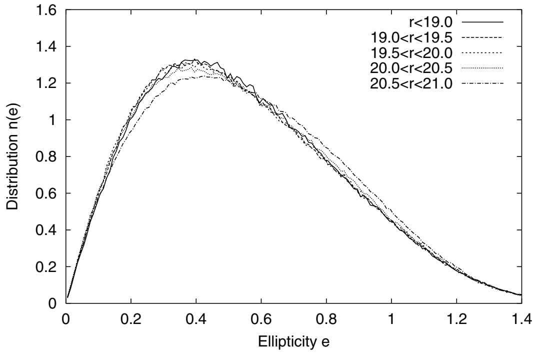

Figure 4. (a) The distribution of measured PSF-corrected ellipticity $\hat{e}^{(f)} = \sqrt{e_+^2 + e_\times^2}$ of source galaxies as a function of r band magnitude. Each curve has been separately normalized to $\int n(e)\,\mathrm{d}e = 1$. (b) The same distribution, except that each galaxy has had noise added to both ellipticity components so that the total noise is $\sigma_e = 0.25$ per component. This allows us to directly compare the various ellipticity distributions, as differences among them are not due to variations in σ_e. A small number (ranging from 0.3 per cent at $r < 19$ to 7 per cent at $20.5 < r < 21.0$) of objects had $\sigma_e > 0.25$; no noise was added to their ellipticities.

For the $20.5 < r < 21.0$ mag range, we compute $\delta\gamma/\gamma = +0.025$. We find that the computed $\delta\gamma/\gamma$ remains between 0.02 and 0.03 as we adjust the order of the fitting polynomial from 4 ($\alpha = 2$) to 20 ($\alpha = 10$), indicating that the polynomial fit is not affecting the results. The error given in Table 1 is 5.0 per cent, which is twice the error obtained from equation (24) (to give a more conservative estimate). We emphasize that we are placing a constraint on the selection bias, and that we have *not* found evidence that this bias is in fact present. In particular, the differences between the curves in Fig. 4(b) could also be due to the small number of objects with large σ_e (so that their ellipticity noises could not be 'boosted' to 0.25); non-Gaussianity of the ellipticity error distribution; systematic errors in ellipticity measurement (perhaps due to PSF effects); a real variation in the source ellipticity distribution with apparent magnitude (as the brighter and fainter galaxies represent distinct populations); or some combination of these effects.

3.2.4 *Shear responsivity error*

Any error in e_{rms} translates into an error in the shear responsivity $\mathcal{R}$ via equation (15) and hence an error in the calibration of equation (14). While the statistical uncertainty in e_{rms} is negligible because we have millions of source galaxies, the systematic uncertainty must be taken into account. An error δe_{rms} thus translates into a calibration error given by:

$$\frac{\delta\gamma}{\gamma} = -\frac{\delta\mathcal{R}}{\mathcal{R}} = \frac{2e_{\mathrm{rms}}\delta e_{\mathrm{rms}}}{1-e_{\mathrm{rms}}^2} \approx 0.86\delta e_{\mathrm{rms}}. \tag{25}$$

From Fig. 3, we take $\delta e_{\mathrm{rms}} = \pm 0.02$ as a reasonable error estimate; if the error in e_{rms} is larger than this then it must either cancel a magnitude dependence of the rms ellipticity or else it must affect objects of all magnitudes similarly (which is unlikely because the resolution factor R_2 is strongly correlated with magnitude; see Fig. 5). This leads to the error estimate from shear responsivity error of $\delta\gamma/\gamma = \pm 0.017$, as given in Table 1.

3.2.5 *Noise-rectification bias*

The fitting to determine $\mathbf{M}^{(I)}$, and the subsequent PSF correction to obtain $\mathbf{e}^{(f)}$, are non-linear operations, hence noise in the original image $I(\boldsymbol{r})$ can lead to a bias in the ellipticity $\mathbf{e}^{(f)}$. The additive bias (spurious power) introduced by noise rectification has been previously noted in the context of cosmic shear surveys (Kaiser 2000; Bernstein & Jarvis 2002). Here we consider the effect of noise rectification on calibration bias. This effect has not been previously analysed, although it is present implicitly in simulations (e.g. Bacon et al. 2001; Erben et al. 2001).

The calibration correction due to noise-rectification bias is proportional to the noise variance and hence to ν^{-2}, where ν is the detection significance of the galaxy, i.e.:

$$\frac{\delta\gamma}{\gamma} \approx K_N \nu^{-2} + O(\nu^{-3}). \tag{26}$$

The noise-rectification coefficient K_N is evaluated in Appendix C, and found to be (compare to equation C27):

$$K_N = 4\left(1 - 3R_2^{-1} + R_2^{-2} + 2e_{\mathrm{rms}}^2\right). \tag{27}$$

Our galaxies have resolution factor $\frac{1}{3} < R_2 < 1$ and $e_{\mathrm{rms}} = 0.37$. Within this range, K_N takes on a minimum value of -3.9 at $R_2 = \frac{2}{3}$ and a maximum value of $+5.1$ at $R_2 = \frac{1}{3}$. A typical $r = 21$ galaxy in moderate (1.7-arcsec FWHM) seeing has $\nu \sim 10, 25$ and 20 in the g, r and i bands, respectively. The bands are weighted by ellipticity error σ_e^{-2}, which is proportional to ν^2 assuming the resolution factors in the three bands are all equal. In this case, the weighted mean ν^{-2} is:

$$\langle \nu^{-2} \rangle_{\mathrm{weighted}} = \frac{3}{\nu_g^2 + \nu_r^2 + \nu_i^2}, \tag{28}$$

which for the signal-to-noise ratios listed above case is 0.0027. The product $K_N \nu^{-2}$ appearing in equation (26) is thus between -0.011 and $+0.014$. This is shown as the upper limit in Table 1.

While the noise-induced calibration bias (equation 26) is a sub-dominant source of error in this investigation, the same may not be true of all lensing observations. For example, for sources detected at 10σ ($\nu = 10$) and resolution factor $R_2 = 0.2$, we find $\delta\gamma/\gamma = +0.44$, which probably dominates the calibration error budget for these sources (see Fig. 6). The lensing studies that use these low-significance objects usually down-weight them due to their large ellipticity uncertainty σ_e, so the noise-induced calibration bias in the final result could still be small. However, in this situation the ellipticity estimator $\hat{\mathbf{e}}^{(f)}$ can be correlated with the weight, which leads to additional terms (positive or negative) in the calibration. The analysis of these correlations and their induced calibration bias is not needed here and is deferred to future work.

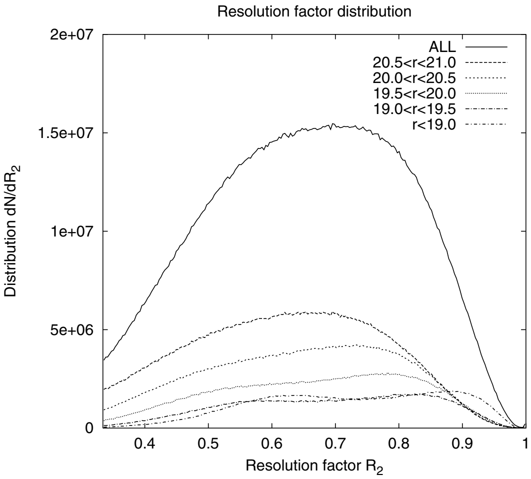

Figure 5. The distribution of source galaxy resolution factors, $\mathrm{d}N/\mathrm{d}R_2 = N_s n(R_2)$.

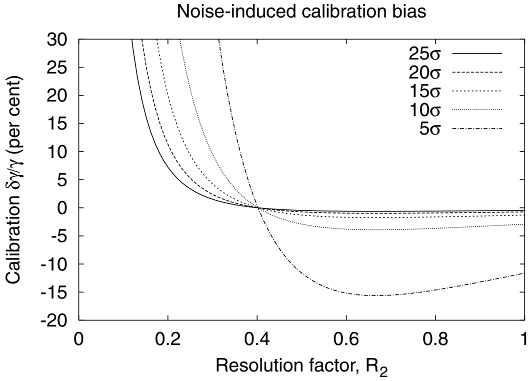

Figure 6. The calibration bias obtained from equation (C27) for $e_{\mathrm{rms}} = 0.37$, as a function of resolution factor R_2 and detection signal-to-noise ratio $\nu = 5, \ldots, 25$. Note the large bias for poor resolution factors $R_2 < 1/3$ and low signal-to-noise ratio. The zero crossing at $R_2 \approx 0.4$ is somewhat dependent on e_{rms} and only exists for the first term in the asymptotic expansion of equation (26), hence this plot should not be taken as an indication that weak lensing measurements are best performed with galaxies of this resolution factor.

3.3 Source photometric redshift samples

It is critical for weak lensing experiments to have accurate knowledge of the source redshifts (and the lens redshifts, in the case of galaxy–galaxy lensing studies). It is also useful for studies of the intrinsic correlations, as it enables us to distinguish physically associated pairs from widely separated pairs for which the gravitational lensing effect dominates the galaxy-apparent shear correlation. In this investigation, we have used spectroscopic redshifts for the lens galaxies and photometric redshifts for the source galaxies. This section describes the methodology used to determine the photometric redshifts, and briefly considers some of tests of the photometric redshifts. Photometric redshift tests will be discussed in more detail in Mandelbaum).

3.3.1 *Methodology*

Photometric redshift algorithms using the five SDSS bandpasses (*u*, *g*, *r*, *i* and *z* centred at 354, 475, 622, 763 and 905 nm, respectively; Fukugita et al. 1996) have previously been developed (Csabai et al. 2003). These photometric redshifts are based on the 'hybrid' photometric redshift methods (Budavári et al. 2000; Csabai et al. 2000), in which the spectral energy distribution (SED) templates are parametrized; the SED parameters and source redshifts are then simultaneously fit to the photometric data. These are only available for some regions of sky (specifically the 2099 deg^2 covered by the SDSS Data Release 1, hereafter DR1). We have therefore used the following methodology to derive photometric redshifts: the DR1 galaxies in our sample are placed in the five-dimensional *ugriz*-space. For each source galaxy outside of the DR1 coverage, we identify the nearest neighbour in *ugriz*-space with a computed photometric redshift:

$$s = \sqrt{(\Delta u)^2 + (\Delta g)^2 + (\Delta r)^2 + (\Delta i)^2 + (\Delta z)^2}. \tag{29}$$

We report a photometric redshift failure if the nearest neighbour lies at distance $s > 0.1$ in *ugriz*-space. Of the 8574 845 galaxies with measured ellipticities and $r < 21$ that pass the flag cuts, matches are found for 6925 528 (including DR1 objects). The separation $s < 0.05$ for 5889 951 of these galaxies, including the 3046 566 galaxies used to construct the nearest-neighbour points.

3.3.2 *Pair ratio tests*

The pair ratio $R_p(r)$ (equation A2) is a useful tool for testing photometric redshifts; it is defined for a given transverse separation and lens luminosity as the ratio of the number density of 'source' galaxies in a given redshift slice at that transverse separation to the number density found in the field. We split the lens–source pairs into widely separated ($z_s > z_l + \epsilon$, where $\epsilon = 0.05$ or 0.1) and nearby ($|z_s - z_l| < \epsilon$) samples. If the photometric redshifts were perfect, we would have $R_p(r) \approx 1$ for the $z_s > z_l + \epsilon$ samples (the exception to this is the magnification bias effect, which should be of the same order of magnitude as the shear, i.e. of the order of 1 per cent). For the $|z_l - z_s| < \epsilon$ samples, we expect $R_p(r) > 1$ due to galaxy clustering.

We compute the pair ratio by dividing the number of lens–source pairs per unit area by the value obtained from randomly generated (Poisson) lens catalogues:

$$R_p(r) = \frac{n(r)}{n_{\mathrm{rand}}(r)}, \tag{30}$$

where $n(r)$ is the number of lens–source pairs per unit area in a given radial bin. The large R_p for the $|z_l - z_s| < \epsilon$ samples is easily seen in Fig. 7, and it is greatly suppressed in the $z_s > z_l + \epsilon$ samples. The density of source galaxies varies considerably with seeing because of our resolution factor and signal-to-noise ratio cuts. If the lens selection algorithm were perfectly independent of seeing, this would not contaminate the pair ratio (which is essentially a cross-correlation between lenses and sources), but slight variations in the lens number density with seeing could cause a systematic effect (positive or negative) on $R_p(r)$. However, in the widely separated samples the combined effect of any seeing systematics and lens–source clustering (due to photometric redshift errors) is $|R_p(r) - 1| < 0.03$ in the innermost bins ($r < 100\ h^{-1}$ kpc) and < 0.01 in the outer bins ($r \sim 1000\ h^{-1}$ kpc). When we split the lenses into different magnitude ranges, we find $|R_p(r) - 1| < 0.03$ in all magnitude ranges except for $M_r < -22$, where R_p ranges from 1.2 (in $30 < r < 100\,h^{-1}$ kpc) to 1.04 (in $300 < r < 992\,h^{-1}$ kpc). This excess is more likely to be a result of photometric redshift errors than systematics in the source density because it is much more significant at small radii and for the brighter lenses. This suggests that the seeing systematic in $R_p(r)$ is at the 1–3 per cent level or less.

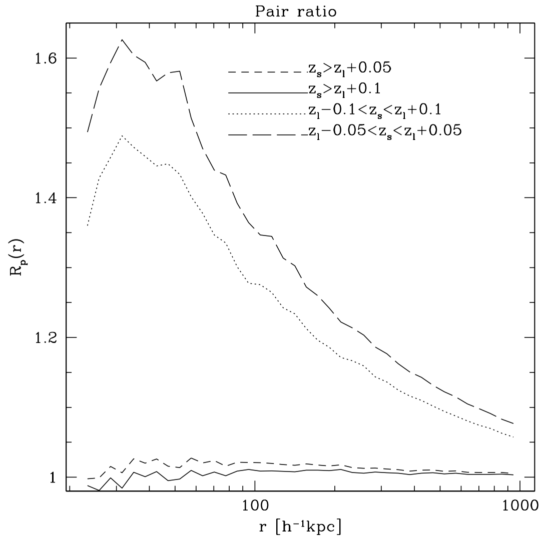

Figure 7. Pair ratio for several samples, as indicated on the plot.

As another test of the photometric redshifts, Fig. 8 shows a plot of the pair ratio for galaxies at $0 < z_s < z_l - \epsilon$. This sample should also include no physically associated pairs, and therefore should have R_p near 1. Instead, there is a large pair ratio at small radii, indicating that some physically associated galaxies at higher redshift are erroneously assigned to very low redshift. (We examined the pair ratio in the range $0.003 < z_s < z_l - \epsilon$ to eliminate objects assigned to very low photometric redshift; this did not reduce the pair ratio, and so we have not imposed this cut in any of the results presented in this paper.) Fortunately, however, the actual number of source galaxies represented by the excess pair ratio in Fig. 8 is relatively small. To see this, we compute the excess number of galaxies in the $0 < z_s < z_l - \epsilon$, $z_l - \epsilon < z_s < z_l + \epsilon$ and $z_s > z_l + \epsilon$ samples:

$$\begin{aligned} N_+ &= (N - N_{\mathrm{rand}})[z_s > z_l + \epsilon] \\ N_0 &= (N - N_{\mathrm{rand}})[z_l - \epsilon < z_s < z_l + \epsilon] \\ N_- &= (N - N_{\mathrm{rand}})[z_s < z_l - \epsilon] \end{aligned} \tag{31}$$

and compute the normalized fractions:

$$f_{+,0,-} = \frac{N_{+,0,-}}{N_+ + N_0 + N_-}. \tag{32}$$

The fractions f_+, f_0 and f_-, respectively, represent the fraction of physically associated source galaxies where the photometric redshifts are overestimated, correctly estimated (to within $\pm\epsilon$) and underestimated. For the sample of all galaxies at radii $30 < r < 446\,h^{-1}$ kpc, we find $f_+ = 0.13$, $f_0 = 0.82$ and $f_- = 0.05$ (for $\epsilon = 0.1$), i.e. only 5 per cent of the source galaxies that are clustered with the lens have redshifts underestimated by more than 0.1. The overestimation and underestimation failure rates increase to

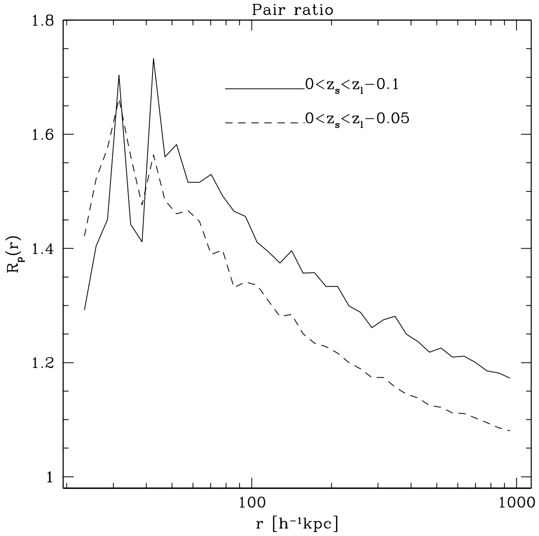

Figure 8. Pair ratio for $0 < z_s < z_l - \epsilon$. Counterintuitively, the $\epsilon = 0.1$ curve is above the $\epsilon = 0.05$ curve; this is because higher-redshift (and hence more luminous due to the apparent magnitude cut for SDSS spectroscopy) lenses are weighted more heavily when we examine only pairs with the 'source' at lower redshift.

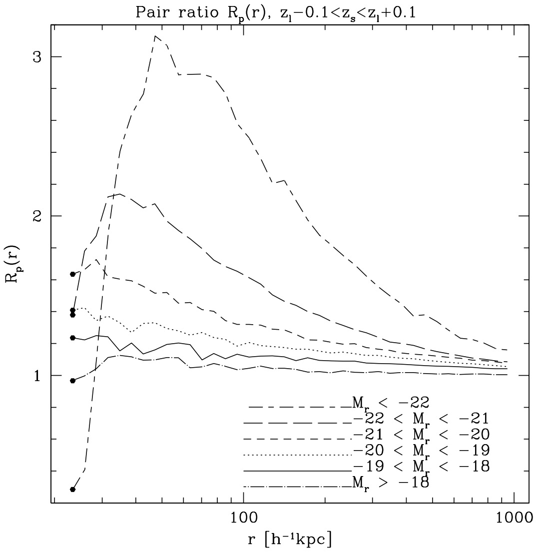

Figure 9. Pair ratio for $|z_s - z_l| < 0.1$, several luminosity subsamples.

$f_+ = 0.26$ and $f_- = 0.16$ if we narrow our redshift slice to $\epsilon = 0.05$. We find that f_- is an increasing function of lens luminosity, which is expected as: (i) the photometric redshift can be an underestimate of the true redshift only if the true redshift exceeds ϵ; and (ii) the more luminous lenses tend to be more distant. Another trend that we find is that the 'probability of correct source photometric redshifts' f_0 decreases with increasing transverse separation r (e.g. for the all lenses, $\epsilon = 0.1$ sample we have $f_0 = 0.90$ at $30 < r < 100\,h^{-1}$ kpc, decreasing to $f_0 = 0.80$ at $300 < r < 446\,h^{-1}$ kpc), which could be indicative of a variation of satellite galaxy colours as a function of radius. The result that $f_+ > f_-$ indicates a bias or skewness in the photometric redshift error distribution.

It thus appears that for the sources used in this paper, roughly 40 per cent of the source galaxies physically associated with a lens are scattered outside of $z_l \pm 0.05$ by photometric redshifts errors, and 20 per cent are scattered outside of $z_l \pm 0.1$.

3.4 Excluded lens–source pairs

At sufficiently small lens–source separation angles, the measurement of sources becomes complicated because the source can overlap with the lens (or with the tail of the PSF convolved with the lens). Problems that occur in this regime can include incorrect ellipticity measurement if overlapping objects are used in the analysis, and selection bias if they are not. In our case deblended objects are not used for ellipticity measurement.

A crude way to determine which annular bins are affected by the overlapping source–lens effect is to examine the pair ratio for source samples selected to be within redshift $|z_s - z_l| < \epsilon$ of the lens (Fig. 9 for $\epsilon = 0.1$). The effect of clustering is easily seen: the pair ratio is greater than unity and (over most of the range of radii) increases as the lens magnitude M_r increases and the transverse separation r decreases. However, at the innermost radii there is a drop off in $R_p(r)$ as sources inside these radii are deblended. Brighter galaxies have a more pronounced dip in the excess at the very innermost radii (out to 40 physical h^{-1} kpc for the very brightest bin), for two reasons: (i) these bright galaxies are typically quite large; and (ii) they are more distant so the same angular separation (relevant to deblending) corresponds to greater physical transverse separation. Padmanabhan et al. (2004) find that for $M_r = -22$ elliptical galaxies (the fainter edge of this brightest luminosity bin), the typical 50 per cent light radius is $10\,h^{-1}$ kpc, in which case there may be significant overlap at the innermost bin ($r = 20\,h^{-1}$ kpc). Since the angular diameter distance is $15 z_l\,h^{-1}$ kpc arcsec^{-1}, and the typical seeing in the SDSS is 1–2 arcsec, the deblending effect can increase the minimum usable radius by tens of h^{-1} kpc for our brightest subsample (typical $z_l \sim 0.25$). For the faintest subsample (typical $z_l \sim 0.03$), this increase is much less important.

Therefore, for the brightest two luminosity samples ($M_r < -21$), we have rejected the inner bins where R_p is increasing with r. (We have verified that rejecting one extra bin or one fewer bin does not significantly affect the final results.)

4 SHEAR UNCERTAINTY ESTIMATION

We use two methods to compute the statistical uncertainty in the shear γ_t. The first is a random lens method, in which we use our source catalogue to compute the covariance of the shear signal around random points within the lens sample region. The second is a bootstrap method in which we cut the lens sample region into 150 subregions that are then resampled. Because both methods use the actual source catalogue, they will correctly take into account error from any spurious shear power in the source catalogue. The random lens method has the disadvantage of not taking into account fluctuations in the lens number density (particularly if they correlate with the noise or systematics in the source catalogue). The bootstrap method addresses these shortcomings on the smallest scales, but suffers due to the fact that the shear signals computed in the 150 subregions are not truly independent, because a source galaxy near a subregion boundary may contribute to the measurement of shear around lenses in multiple subregions. In addition, the noise in the bootstrap covariance matrix (which can have a significant impact on, e.g. χ^2 testing) is more difficult to assess. The bootstrap covariance matrix can be made essentially noiseless by taking thousands of subregions, but then the correlations among the subregions become large and the validity of the bootstrap method is undermined.

Faced with the deficiencies of either the random lens method or the bootstrap method individually, we have chosen to combine them as follows. The errors on the intrinsic alignment determination are computed using both the random-lens and bootstrap covariance matrices; consistency between the two methods suggests that both are reasonable estimates of the uncertainty. The χ^2 analysis is performed using the covariance matrix from the random lens catalogues; the effect of noise in the covariance matrix is taken into account as described in Appendix D. The outermost bins in the faintest luminosity subsamples are excluded from the analysis as galaxy clustering renders the random-lens method inaccurate here, and it is for these bins that the independence of subregions assumed by bootstrap has the least robust justification.

4.1 Random lens method

We compute our statistical errors using a random lens test, which involves computing the shear around randomly located 'lenses', where Poissonian (independent) random lens locations were generated using the angular mask of the survey. We constructed 78 random lens catalogues; the galaxies in each random catalogue were assigned magnitudes and redshifts drawn from the true sample without replacement. The covariance matrix between radial bins i and j is computed as

$$\hat{C}_{ij} = \frac{1}{M-1}\sum_{\alpha=1}^{M}\left[\gamma_t^{(\alpha)}(r_i)\gamma_t^{(\alpha)}(r_j) - \bar{\gamma}_t(r_i)\bar{\gamma}_t(r_j)\right], \tag{33}$$

where $M = 78$ is the number of random catalogues, the index α denotes the random catalogues, and $\bar{\gamma}_t(r_i)$ is the sample mean of the shear in radial bin i averaged over all of the random catalogues. So long as the error distribution of the $\{\gamma_t(r_i)\}$ is jointly Gaussian, $\hat{\mathbf{C}}$ gives an unbiased estimate of the covariance (but it cannot be used naively in χ^2 tests; see Appendix D). The number of random catalogues used must be $\geqslant N$ (the number of radial bins) in order to produce a non-degenerate estimator $\hat{\mathbf{C}}$ for the covariance, but is limited by available processor time.

The Poisson-distributed random lens method produces valid error bars on angular scales where the angular (two-dimensional) galaxy power spectrum is Poisson-dominated and the clustering contribution can be safely neglected. Neglecting edge effects in the survey, this range of angular scales can be determined from the ratio of the galaxy clustering power spectrum to the Poisson spectrum:

$$\psi(k) \equiv \frac{P(k, \text{clustering})}{P(k, \text{Poisson})}$$

$$= \frac{2}{N_{\text{gal}}}\int_0^\infty \frac{\mathrm{d}N_{p,\text{excess}}}{\mathrm{d}r} J_0(kr)\,\mathrm{d}r, \tag{34}$$

where N_{gal} is the number of galaxies in the sample, k is the physical (*not* comoving) wavenumber of interest, r is the transverse separation, and $N_{p,\text{excess}}$ is the number of pairs of galaxies with transverse separation $\leqslant r$ minus the number of pairs derived from a random (Poisson) catalogue. We use the average of the angular diameter distances to the two galaxies for the conversion of angular separation into transverse separation r (this should be valid because no correlations should exist between galaxies at very different angular diameter distances). The ratio $\psi(k)$ is plotted for our samples in Fig. 10.

If we were cross-correlating all of the lens galaxies against the same sample of 'source' galaxies, the error variance of the cross-spectrum would simply be rescaled in proportion to the galaxy power spectrum, i.e. as $\propto 1 + \psi(k)$. (If survey boundary effects can be neglected it does not matter that we are computing the correlation function via pair summation as opposed to via a cross-spectrum in Fourier space.) If $\psi(k) \ll 1$, then the Poisson power spectrum is a good approximation to the lens galaxy power spectrum and hence to the error of γ_t. If $\psi(k) \gg 1$, then the lens galaxy power spectrum is much greater than the Poisson estimate, and the error on γ_t for Poisson-distributed lenses is less than the error for 'real' clustered galaxies. Thus we expect the Poisson random lens method to be a good way to estimate error bars in the case where $\psi(k) \ll 1$. In this paper we are cross-correlating each lens galaxy with the shear of source galaxies within the redshift slice $z_l \pm \epsilon$; this increases the importance of the clustering contribution. However, for each of our luminosity subsamples, the width of the lens redshift distribution Δz is of the order of 2ϵ (or less, for the lowest-luminosity subsamples), hence $\psi(k) \ll 1$ is still a valid condition for the clustering to be unimportant. Since the galaxy power spectrum scales roughly as $P(k, \text{clustering}) \propto k^{-1.2}$, whereas the Poisson contribution is independent of k, the clustering contribution dominates on large scales, whereas the Poisson contribution dominates on small scales. The random lens method is thus valid only at the smaller scales.

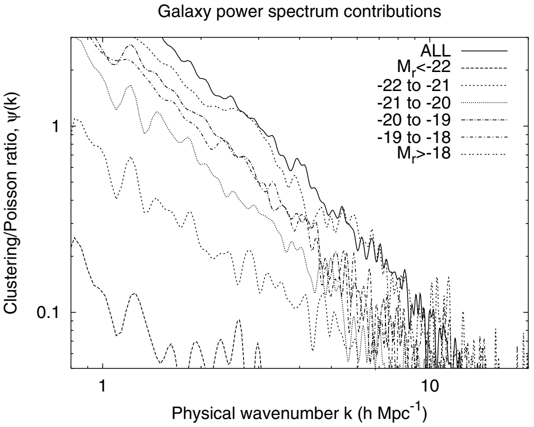

Figure 10. The ratio $\psi(k)$ of clustering to Poisson contributions to the galaxy power spectrum. This is obtained from the data using equation (34), imposing a smooth cut-off in the integrand in the range 20–30 h^{-1} Mpc.

The above reasoning applies in Fourier space. The real-space galaxy-apparent shear correlation function $\gamma_t(r)$ is related to the galaxy-apparent shear cross-power spectrum by:

$$\gamma_t(r) = \frac{1}{2\pi}\int_0^\infty k^2 P_{g\gamma}(k) J_2(kr)\,\mathrm{d}\ln k. \tag{35}$$

The J_2 function peaks at $kr \approx 3.055$; therefore, we take only the annuli out to a distance $r_{\max} = 3.055/k_{\min}$ where $\psi(k_{\min}) = 0.2$. The values of $r_{\max}$ are shown in Table 2.

While the clustering of lens galaxies has the effect of increasing our error bars, the clustering of source galaxies around lens galaxies tends to decrease errors because there are more 'sources' near the lenses in the real catalogue than in the Poisson catalogues. This effect is significant when $R_p - 1$ is of the order of unity (or larger), i.e. in the innermost 200 h^{-1} kpc of our brighter subsamples. It is only important for the source samples where the redshifts are similar to the lens redshifts (the $z_l - \epsilon < z_s < z_l + \epsilon$ samples) as there is negligible lens–source correlation between different redshifts. We have not applied any source clustering correction in the

Table 2. The number of lens galaxies in each luminosity subsample, and the maximum radius $r_{\max}$ at which the Poisson random-catalogue uncertainties are valid. We estimate $r_{\max}$ from $r_{\max} = 3.055/k_{\min}$, where $k_{\min}$ is the minimum wavenumber (largest scale) at which $\psi(k) \leqslant 0.2$, i.e. at which the clustering power spectrum is $\leqslant$20 per cent of the Poisson power spectrum.

Subsample	$N_{\rm gal}$	$r_{\max}$ (h^{-1} Mpc)
All	200 747	0.43
$M_r < -22$	11 337	>1.00
$-22 < M_r \leqslant -21$	54 768	>1.00
$-21 < M_r \leqslant -20$	72 464	0.74
$-20 < M_r \leqslant -19$	41 276	0.55
$-19 < M_r \leqslant -18$	14 475	0.52
$M_r > -18$	6427	0.43

computation of our error bars, thus our error estimates should be viewed as conservative.

4.2 Bootstrap method

The bootstrap method, as applied here, consists of the following major steps.

(i) Split the lens catalogue into $M = 150$ subcatalogues containing similar numbers of lens galaxies.

(ii) Generate $K = 10^5$ synthesized lens catalogues. Each synthesized lens catalogue is a concatenation of $M = 150$ of the subcatalogues, selected randomly with replacement. (Some lens galaxies appear in the synthesized catalogue multiple times, others not at all.)

(iii) Compute the shear signals $\{\gamma_t^{[\alpha]}\}_{\alpha=1}^K$ from each of the synthesized catalogues, and compute their covariance $\hat{\mathbf{C}}_{\rm boot}$.

In order to produce subcatalogues that are as independent as possible, we divide galaxies into subcatalogues that consist of different regions of sky. The subcatalogue boundaries are based on the SDSS λ, η coordinate system (Stoughton et al. 2002). The lens galaxies are first split into 45 rings of width $\Delta\lambda = 4°$ bounded by parallels of constant λ. Within each ring, they are then rank-ordered by η (in the range of -180 to $+180°$). Having arranged the galaxies in this order, we cut the catalogue into 150 approximately equal-sized consecutive groups, which become our subcatalogues. This results in galaxies falling into the same subcatalogue as most of their neighbours. (Some subcatalogues consist of multiple 'islands' in different parts of the survey; we have not attempted any detailed optimization of the subcatalogue cuts.)

The covariance matrix computed via the bootstrap method is noisy even as $K \to \infty$ because a finite number M of subcatalogues has been used. In the extreme case of $M \leqslant N$, the shear signals from each of the subcatalogues would form an M-dimensional plane in the N-dimensional shear space; then the signals computed from bootstrap resampling of these subcatalogues would all lie in this plane and their covariance matrix would be degenerate. As M increases, the noise in the bootstrap covariance matrix goes down, but the samples become less and less independent. We have used $M = 150$ here. Since some of the subcatalogues receive higher weight than others (due to survey geometry, variations in source density, etc.), the calculation of Appendix D cannot be directly applied to the bootstrap method. While this makes χ^2 testing using the bootstrap method difficult, the errors on the final bin-averaged intrinsic alignments obtained from $\hat{\mathbf{C}}_{\rm boot}$ are stable and provide a good check of the correctness of the random-lens errors.

4.3 Chi-squared test

We may test the random-catalogue errors using a χ^2 test, as the γ_{45} shear must (in the mean) vanish by symmetry. At this point, it is essential to note that error covariance matrices obtained from simulations (e.g. as used in this paper) *cannot* be blindly used in place of the true covariance matrices in statistical tests, because they are obtained from a finite number of simulations and hence have a statistical error distribution themselves. In particular, when testing a signal for consistency with zero, it is common to use the χ^2 test, based on the variable:

$$\chi^2_{(45)} = \gamma_{45}^T \mathbf{C}^{-1} \gamma_{45}, \qquad (36)$$

where $\gamma_{45} = [\gamma_{45}(r_1), \ldots, \gamma_{45}(r_N)]$ is the N-dimensional vector of shears in the N radial bins. If γ_{45} is Gaussian-distributed with covariance $\mathbf{C}$ and mean $\mathbf{0}$, then $\chi^2_{(45)}$ has a χ^2 distribution with N degrees of freedom. If we replace $\mathbf{C}$ with the estimate $\hat{\mathbf{C}}$, the distribution of χ^2 becomes much more complicated. This distribution, while analytically intractable, is easy to compute via Monte Carlo simulations (see Appendix D) and we have used this approach for all the p-values quoted in this paper.

We test for zero γ_{45} by computing the statistic $\hat{\chi}^2_{(45)} = \gamma^T_{(45)} \hat{\mathbf{C}}^{-1}_{\rm rand} \gamma_{(45)}$, where $\mathrm{C}_{\rm rand}$ is the error covariance matrix derived from random catalogues. (We put a 'hat' on the $\hat{\chi}^2$ as a reminder that the covariance matrix is noisy, so that this statistic does not have the usual χ^2 distribution; see Appendix D.) The shear data are plotted in Fig. 11(a), while the $\hat{\chi}^2_{(45)}$ values (broken down by lens luminosity) are shown in Table 3 along with their p-values (the cumulative probability of obtaining a lower $\hat{\chi}^2$ assuming that there is indeed zero signal, the errors are Gaussian, and the random realizations correctly sample the error distribution). Out of the 22 subsamples shown in the table, only one has a p-value for the 45°

(a) Mean shear, $z_s > z_l + 0.1$

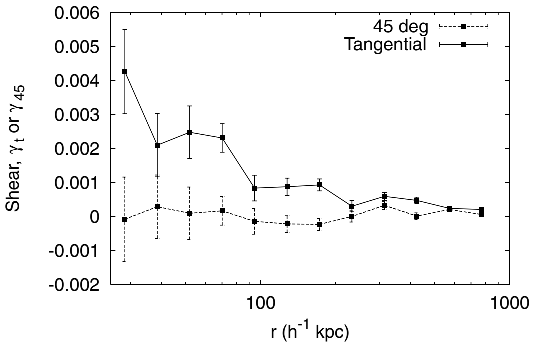

(b) Tangential shear comparison, all magnitudes

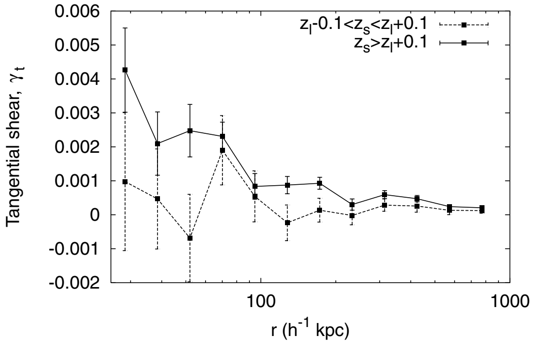

Figure 11. (a) Shear signal for $z_s > z_l + 0.1$. (b) Comparison of tangential shear for pairs widely separated versus nearby in redshift. In both panels we have combined groups of three radial bins for clarity.

Table 3. The $\hat{\chi}^2$ values for fit to zero shear (for both the tangential shear γ_t and the rotated shear γ_{45}) for various lens samples. The p values quoted take into account the effect of noise on the χ^2 calculation as explained in Appendix D, and represent the probability of a random vector having $\hat{\chi}^2$ less than the given value by chance. The number of usable bins (i.e. radial bins where r is large enough to avoid overlap with the lens galaxy but small enough that the clustering contribution is unimportant) is N.

Subsample	N	$\hat{\chi}^2_{(t)}$	$p_{(t)}$	$\hat{\chi}^2_{(45)}$	$p_{(45)}$
		$z_s > z_l + 0.1$			
All	27	179.1	0.999 99	70.8	0.937
$M_r > -18$	29	37.9	0.249	50.5	0.570
$-19 < M_r \leqslant -18$	30	38.2	0.204	42.8	0.313
$-20 < M_r \leqslant -19$	27	67.9	0.922	67.9	0.922
$-21 < M_r \leqslant -20$	34	227.3	0.999 98	65.9	0.568
$-22 < M_r \leqslant -21$	35	160.5	0.997	57.2	0.331
$M_r < -22$	33	154.0	0.998	82.4	0.849
		$\lvert z_s - z_l\rvert < 0.1$			
All	26	39.7	0.489	27.1	0.125
$M_r > -18$	26	31.6	0.244	40.7	0.517
$-19 < M_r \leqslant -18$	28	25.5	0.051	27.9	0.081
$-20 < M_r \leqslant -19$	30	28.3	0.044	21.9	0.007
$-21 < M_r \leqslant -20$	32	85.4	0.901	43.9	0.225
$-22 < M_r \leqslant -21$	33	35.5	0.060	45.1	0.201
$M_r < -22$	30	35.1	0.142	32.6	0.097
		$z_s > z_l + 0.05$			
All	27	213	$> 0.999\,99$	75.3	0.958
$M_r > -19$	27	35.4	0.290	42.6	0.501
$-21 < M_r \leqslant -19$	31	168.8	0.999 90	88.2	0.936
$M_r < -21$	33	244	$> 0.999\,99$	42.7	0.157
		$\lvert z_s - z_l\rvert < 0.05$			
All	26	37.0	0.411	25.1	0.085
$M_r > -19$	26	34.6	0.331	14.2	0.002
$-21 < M_r \leqslant -19$	30	35.6	0.149	28.1	0.043
$M_r < -21$	33	40.9	0.128	55.6	0.424

shear above 0.95, and four have p values above 0.9. These numbers are consistent with the high p-values occurring due to chance. However, the high incidence of low p-values in the $|z_s - z_l| < \epsilon$ (two subsamples have $p_{(45)} < 0.01$) samples requires explanation. This is probably due to conservative assumptions made in computing the errors, particularly the neglect of source–lens clustering, which leads to overestimated errors and therefore lower $\hat{\chi}^2_{(45)}$ and p-values. Because source–lens clustering is more significant for the $|z_s - z_l| < \epsilon$ samples than for the $z_s > z_l + \epsilon$ samples, this explanation is consistent with the fact that the abnormally low p-values occur for the $|z_s - z_l| < \epsilon$ samples. Thus, we conclude that the p-values for the γ_{45} shear show no evidence for systematic effects and suggests that the random-catalogue procedure is not detectably underestimating the error bars.

For completeness, we also show in Table 3 the tangential shear $\hat{\chi}^2_{(t)}$ and p-values. In this case, however, the signal is inconsistent with zero for many of the subsamples, with high p for the brighter luminosity lenses and widely separated ($z_s > z_l + \epsilon$) lens–source pairs. As can be seen from the luminosity-averaged shear signal (Fig. 11), this is because the measured $\gamma_t > 0$ but only for widely separated pairs, consistent with gravitational lensing. Since in this paper we do not fit a model to the lensing shear signal, the tangential $\hat{\chi}^2_{(t)}$ values are not directly useful for establishing the accuracy of error bars.

5 RESULTS

5.1 Intrinsic shear

Table 4 shows the limits on intrinsic shear that can be computed for the various luminosity subsamples and sets of physical radii. The shear was computed by averaging the shear over the range of radii listed, weighting by the total number of lens–source pairs in each radial bin,

$$w_i = \frac{N(r_i)}{\sum_i N(r_i)},$$

$$\Delta\gamma = \frac{N}{N - N_{\mathrm{rand}}} \sum_i w_i \gamma_t(r_i) = \frac{R_p}{R_p - 1} \sum_i w_i \gamma_t(r_i), \tag{37}$$

where N and N_{rand} are summed over all relevant radii to account for the dilution by non-physically associated pairs. The factor of $N/(N - N_{\mathrm{rand}}) = R_p/(R_p - 1)$ is used because intrinsic shear only applies to the excess pairs $N(r_i) - N_{\mathrm{rand}}(r_i)$ (see Appendix A). This number depends on the set of radii and luminosities considered, and as can be seen from Fig. 9, is large for fainter foregrounds and for larger values of radii. (It ranges from close to 50 for the faintest subsamples, down to 1.8 for the brightest subsamples and smallest radii.) Note that shears and errors in all figures have *not* been corrected to account for this dilution effect, and it has no effect on the χ^2 values in Table 3 because the dilution factor cancels out.

The errors on $\Delta\gamma$ were computed using both random catalogues and bootstrap (see Section 4). First, the averaged shear was computed for each of 78 random catalogue outputs (using the same weighting) and $\sigma^{(\mathrm{rand})}$ is the standard deviation of these averaged shears. This random catalogue error was then used to compute the confidence intervals using the Student's t-distribution, which is quite close to Gaussian for 77 degrees of freedom. Secondly, the error from the bootstrap covariance matrices was estimated as

$$\sigma^{(\mathrm{boot})} = \sqrt{\sum_{i,j} w_i w_j C_{\mathrm{boot},ij}} \tag{38}$$

and confidence intervals were computed using a Gaussian distribution (as the noise in the bootstrap covariance matrix $\mathbf{C}_{\mathrm{boot}}$ is unknown). In computing the confidence intervals in Table 4, we used the greater of the two errors (bootstrap or random catalogue).

As a test of consistency, we compared the errors $\sigma^{(\mathrm{rand})}$ and $\sigma^{(\mathrm{boot})}$ computed from the random catalogues and from the bootstrap covariance matrices. For most of the samples shown in the table, the difference between the two error values was less than 25 per cent; the exceptions are the $r < 100\ h^{-1}$ kpc bins for the brighter lens samples, for which the bootstrap errors are smaller than the random catalogue errors. This is probably due to the fact that the number density of source galaxies in the $|z_s - z_l| < \epsilon$ samples is greater near lens galaxies than in the field, hence the shape noise is suppressed. This effect is taken into account by the bootstrap but not by the random catalogues, hence the bootstrap errors are smaller.

A possible source of contamination to the intrinsic alignment signal is gravitational lensing of source galaxies at $z_s > z_l$. We have attempted to estimate the magnitude of such contamination ($10^3 \Delta\gamma_{gl}$ in the table) according to the following procedure. First, the mean value of the inverse critical surface density $\Sigma_c^{-1}(z_s, z_l)$ for each sample was computed, where $\Sigma_c^{-1} = 0$ for $z_s < z_l$. Then, the averaged shear value γ for the radii of interest was computed. The

Table 4. Limits on the tangential intrinsic shear $\Delta\gamma$, for various subsamples and ranges of radii (statistical errors only). The $10^3\Delta\gamma$ column shows the central (most favoured) value. Quantities have been corrected to account for dilution by non-physically associated galaxies in the $|z_s - z_l| < \epsilon$ samples as described in the text. The statistical uncertainties (1σ) on $\Delta\gamma$ are shown in the next two columns for the random-catalogue and bootstrap methods. $\Delta\gamma_{gl}$ is the estimated value of shear for these samples assuming a simple model for contamination by pairs that are actually gravitationally lensed (the errors are 1σ statistical errors on shear measurement only, i.e. they do not include uncertainties associated with the source redshift distribution). The next two columns show the pair ratios R_p for the $|z_s - z_l| < \epsilon$ ('in') and $z_s > z_l + \epsilon$ ('out') samples. Finally, we show confidence intervals for $\Delta\gamma$. The '95 per cent stat.' confidence interval is computed using the central value of $\Delta\gamma - \Delta\gamma_{gl}$ and statistical errors only. The '99.9 per cent stat.+sys.' includes identified systematics as discussed in the text. In the row containing the $[-\infty, +\infty]$ confidence interval, we find no detection of physically associated lens–source pairs when the allowed range of systematic errors is taken into account.

Subsample	r	$10^3\Delta\gamma$	$10^3\sigma(\Delta\gamma)$		$10^3\Delta\gamma_{gl}$	R_p (in)	R_p (out)	$10^3\Delta\gamma$ confidence interval			
			rand	boot				95 per cent stat.		99.9 per cent stat.+sys.	
								min	max	min	max
$\epsilon = 0.1$											
All	[30, 446]	1.6	1.0	1.0	1.45 ± 0.17	1.155	1.008	−1.8	2.1	−6.2	6.6
All	[30, 100]	2.7	2.1	1.7	1.96 ± 0.32	1.355	1.007	−3.4	5.0	−10.5	12.5
All	[100, 300]	−0.4	1.1	1.3	1.26 ± 0.22	1.181	1.010	−4.1	0.8	−9.5	5.1
All	[300, 446]	3.6	1.7	1.6	1.58 ± 0.25	1.120	1.007	−1.4	5.4	−7.4	12.8
$M_r > -18$	[30, 446]	−19.6	14.9	17.7	−0.19 ± 3.05	1.022	0.991	−54.2	15.3	−612.4	305.5
$M_r > -18$	[30, 100]	−18.1	25.4	22.9	9.16 ± 4.20	1.068	0.990	−77.7	23.3	−206.6	115.3
$M_r > -18$	[100, 300]	−24.0	24.6	21.4	−3.13 ± 4.34	1.024	0.991	−69.8	28.1	−412.1	243.1
$M_r > -18$	[300, 446]	−15.5	24.0	31.4	−0.25 ± 5.02	1.017	0.990	−76.7	46.3	$-\infty$	∞
−19 to −18	[27, 493]	−0.7	3.3	3.7	1.52 ± 0.59	1.079	1.013	−9.5	5.1	−28.6	20.8
−19 to −18	[27, 100]	−17.5	9.5	10.0	0.11 ± 1.56	1.148	1.010	−37.3	2.1	−70.2	21.5
−19 to −18	[100, 300]	−6.9	5.4	5.2	1.26 ± 0.88	1.094	1.014	−18.8	2.5	−47.6	19.6
−19 to −18	[300, 493]	6.1	5.0	5.3	1.89 ± 0.86	1.068	1.013	−6.1	14.6	−29.0	45.3
−20 to −19	[33, 545]	1.1	1.8	1.6	1.53 ± 0.33	1.119	1.004	−4.1	3.3	−10.8	9.7
−20 to −19	[33, 100]	6.2	5.2	4.8	1.56 ± 0.78	1.248	1.002	−5.8	15.1	−18.4	29.8
−20 to −19	[100, 300]	−0.7	2.6	2.4	1.28 ± 0.49	1.149	1.007	−7.1	3.1	−15.9	10.7
−20 to −19	[300, 545]	1.6	2.4	2.3	1.67 ± 0.45	1.102	1.004	−4.8	4.7	−12.9	12.8
−21 to −20	[27, 735]	2.6	1.3	1.3	1.18 ± 0.20	1.139	1.011	−1.1	3.9	−5.8	9.8
−21 to −20	[27, 100]	6.6	3.5	2.6	2.59 ± 0.57	1.427	1.007	−3.0	11.0	−13.2	23.2
−21 to −20	[100, 300]	−1.0	2.0	1.8	1.32 ± 0.28	1.217	1.014	−6.2	1.6	−14.1	7.8
−21 to −20	[300, 735]	3.5	1.5	1.6	1.08 ± 0.26	1.119	1.010	−0.8	5.6	−5.8	12.7
−22 to −21	[33, 992]	2.8	1.1	1.2	1.57 ± 0.21	1.146	1.006	−1.1	3.6	−5.7	8.8
−22 to −21	[33, 100]	3.6	3.3	2.3	1.80 ± 0.54	1.807	1.027	−4.8	8.5	−14.4	19.0
−22 to −21	[100, 300]	3.3	1.8	1.8	2.00 ± 0.37	1.355	1.019	−2.2	4.8	−8.9	12.4
−22 to −21	[300, 992]	2.6	1.4	1.6	1.48 ± 0.26	1.121	1.005	−2.0	4.1	−7.2	10.1
$M_r < -22$	[45, 992]	5.3	1.6	1.5	2.25 ± 0.37	1.309	1.048	−0.2	6.4	−7.8	18.0
$M_r < -22$	[45, 100]	−0.6	6.7	3.9	4.59 ± 1.28	2.818	1.204	−18.4	8.0	−43.7	29.8
$M_r < -22$	[100, 300]	3.5	2.8	2.2	2.29 ± 0.53	1.855	1.101	−4.4	6.9	−15.3	18.8
$M_r < -22$	[300, 992]	6.3	1.9	1.8	2.28 ± 0.44	1.246	1.042	0.2	7.8	−8.2	22.1
$\epsilon = 0.05$											
All	[30, 446]	−0.1	0.9	1.2	0.61 ± 0.08	1.201	1.014	−2.9	1.6	−7.1	5.1
All	[30, 100]	−0.7	2.4	1.8	0.97 ± 0.15	1.458	1.022	−6.4	3.0	−14.1	9.7
All	[100, 300]	−1.3	1.2	1.4	0.50 ± 0.10	1.234	1.017	−4.6	0.9	−9.6	4.5
All	[300, 446]	1.5	1.6	1.9	0.68 ± 0.11	1.155	1.012	−2.9	4.4	−8.5	10.7
$M_r > -19$	[30, 446]	−4.5	4.1	4.8	0.51 ± 0.32	1.067	1.004	−14.5	4.4	−29.9	15.8
$M_r > -19$	[30, 100]	−12.2	10.6	9.0	0.87 ± 0.65	1.135	1.005	−34.2	8.0	−65.4	31.2
$M_r > -19$	[100, 300]	−8.4	5.5	5.7	0.00 ± 0.45	1.076	1.006	−19.6	2.8	−38.5	14.7
$M_r > -19$	[300, 446]	1.0	6.8	7.8	0.96 ± 0.54	1.055	1.004	−15.2	15.3	−36.9	36.9
−21 to −19	[25, 545]	−0.4	1.2	1.1	0.58 ± 0.08	1.196	1.015	−3.3	1.4	−7.7	5.1
−21 to −19	[25, 100]	−0.8	3.0	2.6	1.14 ± 0.21	1.469	1.018	−7.8	4.0	−17.0	12.2
−21 to −19	[100, 300]	−2.4	1.5	1.6	0.50 ± 0.12	1.249	1.018	−6.0	0.3	−12.0	4.0
−21 to −19	[300, 545]	0.9	1.7	1.7	0.57 ± 0.11	1.163	1.013	−3.1	3.7	−8.7	9.6
$M_r < -21$	[33, 992]	2.3	1.0	1.0	0.61 ± 0.07	1.253	1.018	−0.4	3.7	−3.4	8.0
$M_r < -21$	[33, 100]	2.0	3.8	2.1	1.00 ± 0.24	2.365	1.100	−6.5	8.5	−16.8	19.5
$M_r < -21$	[100, 300]	2.8	1.7	1.4	0.85 ± 0.13	1.614	1.049	−1.4	5.3	−6.3	11.6
$M_r < -21$	[300, 992]	2.1	1.3	1.2	0.58 ± 0.08	1.209	1.015	−1.0	4.1	−4.7	9.0

estimated contamination is then

$$\Delta\gamma_{gl} = \frac{\Sigma_c^{-1}[|z_s - z_l| < \epsilon]}{\Sigma_c^{-1}[z_s > z_l + \epsilon]}\left(\frac{N}{N - N_{\rm rand}}\right)\gamma[z_s > z_l + \epsilon], \qquad (39)$$

where $N/(N - N_{\rm rand})$ is the dilution factor mentioned previously for the $|z_s - z_l| < \epsilon$ samples. The value $\Delta\gamma_{gl}$ should thus be subtracted from $\Delta\gamma$ in order to yield the correct intrinsic shear. While this calculation gives an estimate of the shear signal due to contamination by lensed pairs, it does not take into account the (currently unknown) photometric redshift error distribution. In particular,

$\Sigma_c^{-1}[|z_s - z_l| < \epsilon]$ is close to zero because the lens–source separation is small, and hence its fractional systematic error may be large (possibly of the order of unity). Values of the shear for $\epsilon = 0.1$ are shown in Fig. 12.

The central values of the confidence intervals in Table 4 labelled '95 per cent stat.' are computed by subtracting the estimated gravitational lensing contamination from the observed intrinsic alignment signal ($\Delta\gamma - \Delta\gamma_{gl}$). The statistical error on $\Delta\gamma_{gl}$ is negligible and has not been included.

The '99.9 per cent stat.+sys.' confidence interval includes, in addition to statistical errors, three of the possible systematic errors: calibration biases in the shear measurement (Section 3.2), errors in the 'correction factor' $R_p/(R_p - 1)$ of equation (37) caused by seeing-induced correlations between high- and low-redshift galaxies (see Section 3.3.2) and systematic errors in $\Delta\gamma_{gl}$ (the statistical errors are negligible). The former is taken into account by dividing the computed shear by a worst-case calibration factor of 0.82 (appropriate if $\delta\gamma/\gamma = -0.18$). The latter is taken into account by assigning to R_p a possible systematic error equal to $2|R_p[\text{out}] - 1|$, where $R_p[\text{out}]$ is the pair ratio for the $z_s > z_l + \epsilon$ sample. This is appropriate as $R_p[\text{out}] = 1$ in the absence of magnification bias, photometric redshift errors, and seeing-induced systematics; it may even be a conservative estimate of seeing-induced systematics because some of the $R_p[\text{out}] > 1$ signal observed for brighter subsamples is probably due to photometric redshift errors. Since the weakest constraints are always obtained from the smallest R_p, we replace R_p in equation (37) with $R_p - 2|R_p[\text{out}] - 1|$. (In the outermost radial bin for the $M_r > -18$ luminosity subsample, this 'minimum value' of R_p is less than one, i.e. when systematic errors are taken into account we do not have a firm detection of clustering of source galaxies around this sample of lenses.) Finally, we allow $\Delta\gamma_{gl}$ to range from zero to twice the measured value, i.e. the 'maximum' value of the confidence interval for $\Delta\gamma$ is computed assuming no gravitational lensing contamination at all, and the 'minimum' value is computed by subtracting $2\Delta\gamma_{gl}$ instead of only $\Delta\gamma_{gl}$ from $\Delta\hat{\gamma}$.

As can be seen from Table 4, we find no evidence for intrinsic alignment of the satellite galaxies (there is a 'detection' at 95 per cent confidence for the $M_r < -22$ subsample at $45 < r < 100\,h^{-1}$ kpc, but given the large number of subsamples investigated this should not be taken as evidence for $\Delta\gamma \neq 0$). With all samples averaged together, we find conservatively that $-0.0062 < \Delta\gamma < +0.0066$, although we cannot exclude the possibility of a large intrinsic alignment if present around only the faintest 'lens' galaxies.

5.2 Systematic shear

Table 5 includes limits on the systematic shear, i.e. the additive bias contributed by observational systematics to the total shear. Such a contribution could arise if, e.g. there were a correlation between the PSF and the survey boundaries. These limits were computed by taking the average value of the shears computed from the 78 random catalogues, and finding confidence intervals around this average using the Student's t-distribution with 77 degrees of freedom (dividing σ by $\sqrt{78}$ because the measurement was performed with 78 random catalogues). As shown, the systematic shear is consistent with zero for all samples; furthermore it is negligible compared with the statistical error in $\Delta\gamma$, as can be seen by comparing the upper limits in Table 5 to the statistical errors shown in Table 4. A plot of the systematic shear is shown in Fig. 13.

Table 5. Limits on systematic shear in the source catalogue $10^5\Delta\gamma_S$ for various subsamples and ranges of radii. Values are quoted using the errors computed from random catalogues (rand), at 95 and 99.9 per cent confidence level, using the Student's t-distribution (with errors divided by $\sqrt{78}$ because there are 78 measurements of systematic shear).

Subsample	r	$10^5\,\Delta\gamma_{\mathrm{S(rand)}}$	
M_r	(h^{-1} kpc)	95 per cent	99.9 per cent
		$\epsilon = 0.1$	
All	[30, 446]	[−3.1, 2.7]	[−5.2, 4.8]
All	[30, 100]	[−4.6, 20.2]	[−13.5, 29.1]
All	[100, 300]	[−5.6, 1.8]	[−8.2, 4.4]
All	[300, 446]	[−3.8, 4.4]	[−6.8, 7.4]
> -18	[30, 446]	[−1.5, 13.1]	[−6.7, 18.3]
> -18	[30, 100]	[−13.3, 59.9]	[−39.5, 86.1]
> -18	[100, 300]	[−5.2, 21.2]	[−14.6, 30.6]
> -18	[300, 446]	[−6.2, 11.4]	[−12.6, 17.8]
−19 to −18	[27, 493]	[−6.9, 3.9]	[−10.8, 7.8]
−19 to −18	[27, 100]	[−14.3, 40.9]	[−34.1, 60.7]
−19 to −18	[100, 300]	[−9.5, 11.3]	[−16.9, 18.7]
−19 to −18	[300, 493]	[−11.0, 3.4]	[−16.1, 8.5]
−20 to −19	[33, 545]	[−5.8, 3.0]	[−9.0, 6.2]
−20 to −19	[33, 100]	[−21.7, 25.3]	[−38.5, 42.1]
−20 to −19	[100, 300]	[−10.0, 5.0]	[−15.3, 10.3]
−20 to −19	[300, 545]	[−6.1, 3.9]	[−9.7, 7.5]
−21 to −20	[27, 735]	[−4.6, 2.4]	[−7.1, 4.9]
−21 to −20	[27, 100]	[−17.7, 29.7]	[−34.7, 46.7]
−21 to −20	[100, 300]	[−11.9, 3.9]	[−17.5, 9.5]
−21 to −20	[300, 735]	[−4.3, 2.9]	[−6.9, 5.5]
−22 to −21	[33, 992]	[−2.4, 3.6]	[−4.6, 5.8]
−22 to −21	[33, 100]	[−32.3, 34.7]	[−56.4, 58.8]
−22 to −21	[100, 300]	[−20.3, 0.7]	[−27.8, 8.2]
−22 to −21	[300, 992]	[−1.6, 5.0]	[−4.1, 7.5]
< -22	[45, 992]	[−9.7, 7.7]	[−16.0, 14.0]
< -22	[45, 100]	[−120.7, 72.7]	[−190.1, 142.1]
< -22	[100, 300]	[−32.7, 26.3]	[−53.9, 47.5]
< -22	[300, 992]	[−8.6, 8.2]	[−14.7, 14.3]
		$\epsilon = 0.05$	
All	[30, 446]	[−4.1, 2.7]	[−6.6, 5.2]
All	[30, 100]	[−5.4, 28.2]	[−17.4, 40.2]
All	[100, 300]	[−5.9, 3.9]	[−9.4, 7.4]
All	[300, 446]	[−6.6, 3.2]	[−10.1, 6.7]
> -19	[30, 446]	[−3.7, 8.1]	[−7.9, 12.3]
> -19	[30, 100]	[−11.6, 45.0]	[−31.9, 65.3]
> -19	[100, 300]	[−2.9, 14.7]	[−9.2, 21.0]
> -19	[300, 446]	[−9.9, 6.3]	[−15.6, 12.0]
−21 to −19	[25, 545]	[−7.8, 0.8]	[−10.9, 3.9]
−21 to −19	[25, 100]	[−1.0, 41.8]	[−16.4, 57.2]
−21 to −19	[100, 300]	[−11.6, 2.0]	[−16.6, 7.0]
−21 to −19	[300, 545]	[−9.7, 1.1]	[−13.6, 5.0]
< -21	[33, 992]	[−5.1, 4.1]	[−8.5, 7.5]
< -21	[33, 100]	[−74.1, 24.1]	[−109.3, 59.3]
< -21	[100, 300]	[−18.6, 10.0]	[−28.9, 20.3]
< -21	[300, 992]	[−4.6, 5.4]	[−8.2, 9.0]

6 DISCUSSION

In this paper, we have set stringent new limits on intrinsic alignments as a contaminant of the galaxy–galaxy lensing signal. For example, averaging together all lens galaxies at radii out to $446\,h^{-1}$ kpc we derive $-0.0062 < \Delta\gamma < +0.0066$ (99.9 per cent confidence including identified systematics; see Table 4) or $-0.0018 < \Delta\gamma < +0.0021$ (95 per cent confidence, statistical errors only). The statistical constraint is a factor of ∼5 (∼1.5 for our more

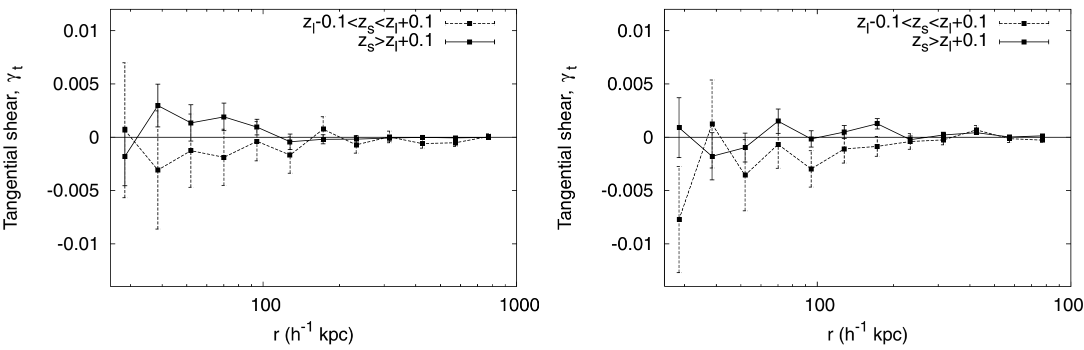
(a) Tangential shear comparison, $M_r > -18$

(b) Tangential shear comparison, $-19 < M_r < -18$

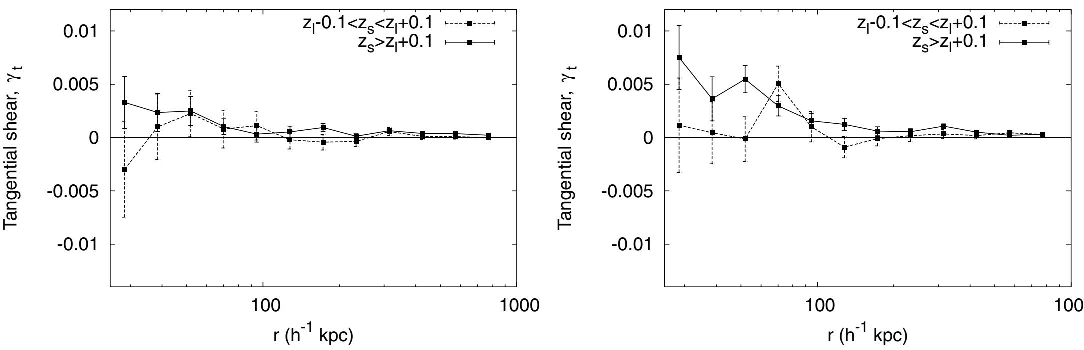
(c) Tangential shear comparison, $-20 < M_r < -19$

(d) Tangential shear comparison, $-21 < M_r < -20$

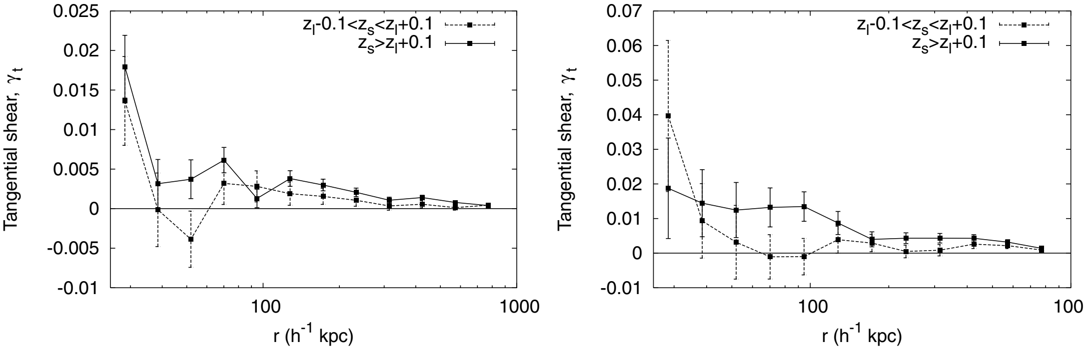
(e) Tangential shear comparison, $-22 < M_r < -21$

(f) Tangential shear comparison, $M_r < -22$

Figure 12. Shear as a function of radial pair separation; panels (a)–(f) show the six luminosity bins in order of increasing luminosity. The solid line shows the widely separated lens–source pairs ($z_s - z_l > 0.1$) and the dashed line shows the nearby pairs ($|z_s - z_l| < 0.1$). Each point on the plot shows three of our radial bins averaged together to increase the signal-to-noise ratio for visual inspection. Note that the vertical scales are increased for panels (e) and (f).

conservative error bar) tighter than $|\Delta\gamma| \leqslant 0.01$ (95 per cent confidence) as obtained from APM/2dF data by Bernstein & Norberg (2002). It also extends to smaller radii than the measurements of nearby spirals by Lee & Pen (2001). Furthermore, our study of the luminosity and radius dependence of the intrinsic shear is useful for weak lensing studies that divide lens galaxies into luminosity subsamples.

Our limits have been obtained by using ‘lens’ galaxies with spectroscopic redshifts and ‘source’ galaxies with photometric redshifts, a different strategy than that selected by previous observers (Lee & Pen 2001; Bernstein & Norberg 2002) who used lens–source pairs selected entirely on the basis of spectroscopic redshift information. This strategy has dramatically increased our sample size and reduced our statistical uncertainties for the brighter lenses ($M_r < -20$) because these are typically at redshift $z > 0.1$, where most of their satellites are too faint to be targeted by SDSS spectroscopy. This method does, however, have disadvantages. For our fainter-luminosity lenses, the photometric-redshift source method gives very large error bars (Table 4) because there are few physically associated lens–source pairs and hence any intrinsic alignment signal will be drowned out by the large number of unassociated pairs. The use of photometrically selected pairs also comes with the caveat that the limits on $\Delta\gamma$ could be circumvented by a small class of galaxies that have strong intrinsic alignments but always produce incorrect photometric redshifts. It is thus recommended that the values in Table 4 with redshift slice half-width $\epsilon = 0.1$ be used to constrain intrinsic alignments in galaxy–galaxy lensing studies, as in this case only approximately 20 per cent of the physically associated source galaxies are scattered out of the sample by photometric redshift errors.

Despite the recent interest in intrinsic alignments as a contaminant of cosmic shear (i.e. shear–shear correlations), there has been comparatively little theoretical work on the density-shear correlation. Lee & Pen (2001) do provide a prediction for the

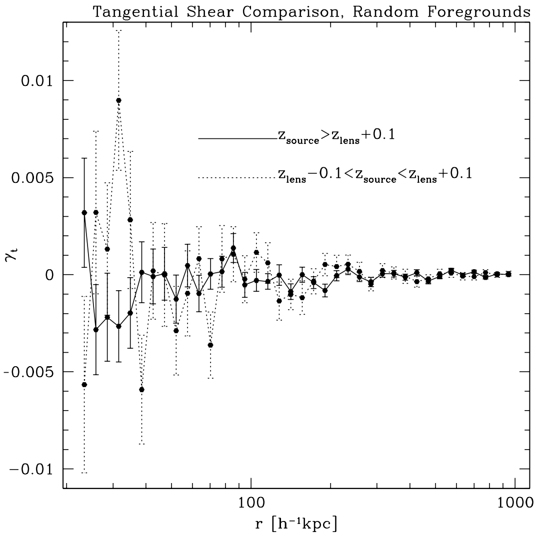

Figure 13. The tangential shear signal computed around one of the random lens catalogues.

density-shape correlation for spiral 'source' galaxies, which we convert (see Appendix B) to $\Delta\gamma = -0.004$ at small radii $r < 1\,h^{-1}$ Mpc. This is marginally consistent with our results (it is within our more conservative confidence interval of $-0.0062 < \Delta\gamma < +0.0066$), although the comparison is imperfect as the model applies only to spiral sources. More generally, measurements of the density-shear correlation $\Delta\gamma$ provide a constraint on intrinsic alignment models in addition to that provided by the shear autocorrelation measurements (Pen et al. 2000; Brown et al. 2002). It would thus be useful to compute the predictions of other intrinsic alignment models for $\Delta\gamma$ and determine which models agree with the intrinsic shear measurements presented here and in Bernstein & Norberg (2002).

We conclude by roughly estimating the intrinsic alignment contamination to the gravitational lensing shear, $(1 - R_p^{-1})\Delta\gamma$. For example, if our source catalogue restricted to $z_s > z_l + 0.1$ were used in a lensing study of the haloes of SDSS spectroscopic galaxies, we would have a contamination fraction $1 - R_p^{-1} \sim 0.01$ in the $100 < r < 300$ h^{-1} kpc bin and intrinsic alignment contamination $|\Delta\gamma| < 0.0095$ (see Table 4), corresponding to a contamination to the gravitational lensing shear at the level of $< 9.5 \times 10^{-5}$. This is approximately equal to the size of the 1σ error bars at these radii for our full sample (1.0×10^{-4}; see Fig. 11) and a factor of 6 less than the shear signal, $\sim 5.8 \times 10^{-4}$. Slightly weaker constraints are placed on the intrinsic alignments around the brighter lenses, but in these cases the lensing signal is a factor of several higher, e.g. for the $-21 > M_r > -22$ mag range we have $|\Delta\gamma| < 0.0124$ at $100 < r < 300\,h^{-1}$ kpc, $1 - R_p^{-1} \sim 0.02$, and shear signal $\gamma_t = 2 \times 10^{-3}$, so the contamination is at worst approximately a factor of 8 smaller than the signal. These results indicate at 99.9 per cent confidence that, except possibly for the faintest lens galaxies, intrinsic alignments are only contaminating the subMpc scale galaxy–galaxy lensing signal at the $\lesssim$15 per cent level.

ACKNOWLEDGMENTS

We acknowledge useful discussions with James Gunn, Zeljko Ivezić, Yeong-Shang Loh, Robert Lupton, Patrick McDonald and Michael Strauss.

C.H. is supported by a NASA Graduate Student Researchers Program (GSRP) fellowship. R.M. is supported by an NSF Graduate Research Fellowship. U.S. is supported by Packard Foundation, Sloan Foundation, NASA NAG5-1993 and NSF CAREER-0132953.

Funding for the creation and distribution of the SDSS Archive has been provided by the Alfred P. Sloan Foundation, the Participating Institutions, the National Aeronautics and Space Administration, the National Science Foundation, the U.S. Department of Energy, the Japanese Monbukagakusho, and the Max Planck Society. The SDSS Web site is http://www.sdss.org/.

The SDSS is managed by the Astrophysical Research Consortium (ARC) for the Participating Institutions. The Participating Institutions are The University of Chicago, Fermilab, the Institute for Advanced Study, the Japan Participation Group, The Johns Hopkins University, Los Alamos National Laboratory, the Max-Planck-Institute for Astronomy (MPIA), the Max-Planck-Institute for Astrophysics (MPA), New Mexico State University, University of Pittsburgh, Princeton University, the United States Naval Observatory and the University of Washington.

REFERENCES

Abazajian K. et al., 2003, AJ, 126, 2081
Abazajian K. et al., 2004, AJ, in press (astro-ph/0403325)
Bacon D.J., Refregier A.R., Ellis R.S., 2000, MNRAS, 318, 625
Bacon D.J., Refregier A., Clowe D., Ellis R.S., 2001, MNRAS, 325, 1065
Bartelmann M., Schneider P., 2001, Phys. Rep., 340, 291
Bernstein G.M., Jarvis M., 2002, AJ, 123, 583
Bernstein G.M., Norberg P., 2002, AJ, 124, 733
Blanton M.R., Lin H., Lupton R.H., Maley F.M., Young N., Zehavi I., Loveday J., 2003a, AJ, 125, 2276
Blanton M.R. et al., 2003b, AJ, 125, 2348
Brainerd T.G., Blandford R.D., Smail I., 1996, ApJ, 466, 623
Brown M.L., Taylor A.N., Hambly N.C., Dye S., 2002, MNRAS, 333, 501
Brown M.L., Taylor A.N., Bacon D.J., Gray M.E., Dye S., Meisenheimer K., Wolf C., 2003, MNRAS, 341, 100
Budavári T., Szalay A.S., Connolly A.J., Csabai I., Dickinson M., 2000, AJ, 120, 1588
Catelan P., Kamionkowski M., Blandford R.D., 2001, MNRAS, 320, L7
Colless M. et al., 2001, MNRAS, 328, 1039
Crittenden R.G., Natarajan P., Pen U., Theuns T., 2001, ApJ, 559, 552
Croft R.A.C., Metzler C.A., 2000, ApJ, 545, 561
Csabai I., Connolly A.J., Szalay A.S., Budavári T., 2000, AJ, 119, 69
Csabai I. et al., 2003, AJ, 125, 580
Erben T., Van Waerbeke L., Bertin E., Mellier Y., Schneider P., 2001, A&A, 366, 717
Finkbeiner D. et al. 2004, AJ, submitted
Fischer P., Tyson J.A., 1997, AJ, 114, 14
Fischer P. et al., 2000, AJ, 120, 1198
Fukugita M., Ichikawa T., Gunn J.E., Doi M., Shimasaku K., Schneider D.P., 1996, AJ, 111, 1748
Gunn J.E. et al., 1998, AJ, 116, 3040
Guzik J., Seljak U., 2002, MNRAS, 335, 311
Heavens A., Refregier A., Heymans C., 2000, MNRAS, 319, 649
Heymans C., Brown M., Heavens A., Meisenheimer K., Taylor A., Wolf C., 2004, MNRAS, 347, 895
Hirata C.M., Seljak U., 2003, MNRAS, 343, 459
Hoekstra H., 2004, MNRAS, 347, 1337
Hoekstra H., Franx M., Kuijken K., Squires G., 1998, ApJ, 504, 636
Hoekstra H., Franx M., Kuijken K., 2000, ApJ, 532, 88
Hoekstra H. et al., 2001, ApJ, 548, 5
Hoekstra H., Yee H.K.C., Gladders M.D., Barrientos L.F., Hall P.B., Infante L., 2002, ApJ, 572, 55
Hoekstra H., Franx M., Kuijken K., Carlberg R.G., Yee H.K.C., 2003, MNRAS, 340, 609
Hoekstra H., Yee H.K.C., Gladders M.D., 2004, ApJ, 606, 67
Hogg D.W., Finkbeiner D.P., Schlegel D.J., Gunn J.E., 2001, AJ, 122, 2129
Hudson M.J., Gwyn S.D.J., Dahle H., Kaiser N., 1998, ApJ, 503, 531

Hui L., Zhang J., 2002, preprint (astro-ph/0205212)
Jarvis M., Bernstein G.M., Fischer P., Smith D., Jain B., Tyson J.A., Wittman D., 2003, AJ, 125, 1014
Jing Y.P., 2002, MNRAS, 335, L89
Kaiser N., 2000, ApJ, 537, 555
Kaiser N., Squires G., Broadhurst T., 1995, ApJ, 449, 460
Lee J., Pen U., 2000, ApJ, 532, L5
Lee J., Pen U., 2001, ApJ, 555, 106
Lee J., Pen U., 2002, ApJ, 567, L111
Luppino G.A., Kaiser N., 1997, ApJ, 475, 20
Lupton R., Gunn J.E., Ivezić Z., Knapp G.R., Kent S., Yasuda N., 2001, in Harnden F.R., Jr, Primini F.A., Payne H.E., eds, ASP Conf. Ser. Vol. 238, Astronomical Data Analysis Software and Systems X. Astron. Soc. Pac., San Francisco, p. 269
McKay T.A. et al., 2001, preprint (astro-ph/0108013)
Maddox S.J., Efstathiou G., Sutherland W.J., Loveday J., 1990, MNRAS, 243, 692
Miralda-Escudé J., 1991, ApJ, 380, 1
Padmanabhan N. et al., 2004, New Astron., 9, 329
Pen U., Lee J., Seljak U., 2000, ApJ, 543, L107
Pier J.R., Munn J.A., Hindsley R.B., Hennessy G.S., Kent S.M., Lupton R.H., Ivezić Ž., 2003, AJ, 125, 1559
Refregier A., 2003a, ARA&A, 41, 645
Refregier A., 2003b, MNRAS, 338, 35
Refregier A., Bacon D., 2003, MNRAS, 338, 48
Rhodes J., Refregier A., Groth E.J., 2001, ApJ, 552, L85
Schlegel D.J., Finkbeiner D.P., Davis M., 1998, ApJ, 500, 525
Sheldon E.S. et al., 2001, ApJ, 554, 881
Sheldon E.S. et al., 2004, AJ, 127, 2544
Smith D.R., Bernstein G.M., Fischer P., Jarvis M., 2001, ApJ, 551, 643
Smith J.A. et al., 2002, AJ, 123, 2121
Spergel D.N. et al., 2003, ApJS, 148, 175
Stoughton C. et al., 2002, AJ, 123, 485
Strauss M.A. et al., 2002, AJ, 124, 1810
Van den Bosch F.C., Abel T., Croft R.A.C., Hernquist L., White S.D.M., 2002, ApJ, 576, 21
Van Waerbeke L. et al., 2000, A&A, 358, 30
Van Waerbeke L., Mellier Y., Pelló R., Pen U.-L., McCracken H.J., Jain B., 2002, A&A, 393, 369
York D.G. et al., 2000, AJ, 120, 1579

APPENDIX A: INTRINSIC SHEAR AND CORRELATION FUNCTION

In principle, the tangential component of intrinsic shear $\Delta\gamma_t$ is a function not only of the transverse separation r between the lens and source galaxy, but also on the line-of-sight separation u. The contribution of the intrinsic alignments to the shear $\hat{\gamma}_t$ observed in galaxy–galaxy weak lensing is:

$$\hat{\gamma}_t(\mathrm{intr}, r) = \frac{\int \Delta\gamma_t(r, u) n(r, u)\,\mathrm{d}u}{\int n(r, u)\,\mathrm{d}u}, \tag{A1}$$

where $n(r, u)\ \mathrm{d}u\ \ \mathrm{d}^2\boldsymbol{r}$ is the number of sources with line-of-sight separation between u and $u + \mathrm{d}u$ in area $\mathrm{d}^2\boldsymbol{r}$ in the lens plane. This contamination is typically estimated by comparing the total number of sources observed per unit area in the lens plane, i.e. $\int n(r, u)\,\mathrm{d}u$, to the number of sources observed in a randomly selected field, $\int n(\infty, u)\,\mathrm{d}u$. We express this in terms of a 'pair ratio' $R_p(r)$:

$$R_p(r) = \frac{\int n(r, u)\,\mathrm{d}u}{\int n(\infty, u)\,\mathrm{d}u}. \tag{A2}$$

The simplest interpretation of the pair ratio is that the fraction of the source galaxies that are physically unassociated with the lens is R_p^{-1}, and that the remaining fraction $1 - R_p^{-1}$ are physically associated with the lens. This motivates the definition of the projected intrinsic shear $\Delta\gamma(r)$ of physically associated galaxies as

$$\Delta\gamma(r) \equiv \frac{\hat{\gamma}_t(\mathrm{intr}, r)}{1 - R_p^{-1}}. \tag{A3}$$

Most analyses of the effect of intrinsic alignments on galaxy–galaxy lensing studies (e.g. Bernstein & Norberg 2002; Sheldon et al. 2004) have used equation (A3) to compute $\hat{\gamma}_t(\mathrm{intr})$ from the measured pair ratio R_p and an estimate of the intrinsic shear of physically associated galaxies $\Delta\gamma(r)$ based on spectroscopically selected lens–source pairs at the same redshift.

While equation (A3) is directly useful for measuring the intrinsic alignment and estimating the contamination of weak-lensing results, we can also write $\Delta\gamma(r)$ in terms of a projection integral along the line of sight. Substituting equations (A1) and (A2) into equation (A3), we find:

$$\Delta\gamma(r) = \frac{\int \Delta\gamma_t(r, u) n(r, u)\,\mathrm{d}u}{\int [n(r, u) - n(\infty, u)]\,\mathrm{d}u}. \tag{A4}$$

The integrands in both the numerator and denominator of equation (A4) vanish at large $|u|$ (so long as the magnification bias due to gravitational lensing is small). At small $|u|$ [i.e. much less than the typical distance to the lenses, so that variations in $n(\infty, u)$ can be ignored], $n(r, u)$ is related to the galaxy–galaxy correlation function via $n(r, u) \propto 1 + \xi(\sqrt{r^2 + u^2})$. Therefore, we may write

$$\Delta\gamma(r) = \frac{\int \Delta\gamma_t(r, u)[1 + \xi(\sqrt{r^2 + u^2})]\,\mathrm{d}u}{\int \xi(\sqrt{r^2 + u^2})\,\mathrm{d}u}, \tag{A5}$$

which is the relation of $\Delta\gamma(r)$ to fundamental (as opposed to observed) quantities.

APPENDIX B: RELATION OF INTRINSIC SHEAR TO POSITION ANGLE STATISTICS

Lee & Pen (2000) and Lee & Pen (2001) measure density-shape correlations using the position angle statistic,

$$\omega_{2D}(r_{3D}) \equiv \langle \cos^2\phi \rangle - \frac{1}{2} = \frac{1}{2}\langle \cos 2\phi \rangle, \tag{B1}$$

where ϕ is the position angle of the minor axis of the source galaxy relative to the lens (0 indicates radial alignment, $\pi/2$ tangential alignment) and the three-dimensional pair separation is $r_{3D} = \sqrt{r^2 + u^2}$. Lee & Pen (2001) consider spiral galaxies and hence interpret the minor axis as the (projected) rotation axis of the galaxy, but equation (B1) is what is directly measured.

We consider here a crude model for the conversion between ω_{2D} and the intrinsic shear $\Delta\gamma$. Formulae for the transformation of ellipticity under shear are given by Miralda-Escudé (1991); using that $\tan 2\phi = e_{45}/e_t$ (in a coordinate system aligned with the direction to the lens galaxy) we can find the transformation of the position angle under shear,

$$\frac{\partial\phi}{\partial\gamma_t} = -e^{-1}\sin 2\phi. \tag{B2}$$

Substitution into equation (B1) yields

$$\frac{\mathrm{d}\omega_{2D}}{\mathrm{d}\gamma_t} = \frac{1}{2}\left\langle (-e^{-1}\sin 2\phi)\frac{\mathrm{d}}{\mathrm{d}\phi}\cos 2\phi \right\rangle = \frac{1}{2}\langle e^{-1} \rangle. \tag{B3}$$

We define this quantity to be the position angle responsivity $\mathcal{R}_\omega$; for our $r < 19$ galaxies (with negligible measurement noise in the ellipticity), $\langle e^{-1} \rangle = 2.75$ and $\mathcal{R}_\omega = 1.38$. The theory of Lee & Pen (2001) suggests that at small radii ($r_{3D} < 1.5\ h^{-1}$ Mpc) we should have $\omega_{2D}(r) = -0.0057$ for spirals (see their fig. 2) or $\gamma_t = \omega_{2D}/\mathcal{R}_\omega = -0.0041$. Since the galaxy autocorrelation function $\xi(r_{3D}) \gg 1$ at these radii, we expect $\Delta\gamma = -0.0041$ (cf. Equation A5). This conversion is only a rough estimate as the relation equation (B3) between ω_{2D} and γ_+ was derived for a gravitational shear, and it need not be the correct relation for intrinsic shear.

Using the conversion $\mathcal{R}_\omega = 1.38$, the data presented in fig. 2 of Lee & Pen (2001) correspond to $\Delta\gamma = -0.0037 \pm 0.0025$ at $r_{3D} = 500\,h^{-1}$ kpc.

APPENDIX C: NOISE-RECTIFICATION BIAS

Noise in galaxy images has several effects for weak lensing. The best-known effect is the introduction of measurement noise in the ellipticity. It has also been pointed out that noise can also couple to the PSF anisotropy to produce spurious power in cosmic shear measurements, even if the PSF correction is otherwise exact (Kaiser 2000; Bernstein & Jarvis 2002). This occurs because of a noise-rectification bias, i.e. the ellipticity is a non-linear function of the image intensity so that an unbiased estimate of the intensity need not translate into an unbiased estimate of the ellipticity. Here we estimate the effect of noise-rectification biases on the shear calibration of low signal-to-noise ratio galaxies.

Our plan for approaching this problem is as follows.

(i) Determine, for a circular Gaussian galaxy with unit radius $\sigma = 1$ and unit central intensity $I(0) = 1$, the mean and covariance of the measured adaptive moments $\hat{\mathbf{M}}^{(I)}$ to leading order in the noise.

(ii) Use scaling and symmetry principles to derive the mean and covariance of $\hat{\mathbf{M}}^{(I)}$ for a general elliptical Gaussian galaxy.

(iii) Propagate these errors to the PSF-corrected ellipticity $\hat{\mathbf{e}}^{(f)}$.

Here we will neglect corrections due to non-Gaussianity of the galaxy or PSF.

We first introduce some notation. We write the normalization, centroid and moments of the galaxy as a six-dimensional vector:

$$c^\alpha = \left(A, x_0, y_0, [M^{-1}]^{xx}, [M^{-1}]^{xy}, [M^{-1}]^{yy}\right). \tag{C1}$$

(We could have used the matrix elements of $\mathbf{M}$ to parametrize the family of Gaussians instead of $\mathbf{M}^{-1}$; however, using $\mathbf{M}^{-1}$ simplifies the algebra.) We now introduce the notation:

$$J(\boldsymbol{r}; c^\alpha) = A \exp - \frac{(\boldsymbol{r} - \boldsymbol{r}_0)^T \mathbf{M}^{-1} (\boldsymbol{r} - \boldsymbol{r}_0)}{2}. \tag{C2}$$

Thus the energy functional equation (1) becomes

$$E(c^\alpha; I) = \frac{1}{2} \int [I(\boldsymbol{r}) - J(\boldsymbol{r}, c^\alpha)]^2 \, \mathrm{d}^2\boldsymbol{r}; \tag{C3}$$

or, written as an inner product:

$$E(c^\alpha; I) = \frac{1}{2} \langle I - J, I - J \rangle \tag{C4}$$

(we suppress the c^α argument of J for clarity). Minimizing this yields:

$$0 = \langle I - J, J_\alpha \rangle, \tag{C5}$$

where $J_\alpha \equiv J/c^\alpha$.

We may obtain the dependence of c^α on I by taking the functional derivative of equation (C5) with respect to $I(\boldsymbol{r}_1)$:

$$0 = J_\alpha(\boldsymbol{r}_1) + (\langle I - J, J_{\alpha\beta} \rangle - \langle J_\beta, J_\alpha \rangle) \frac{\mathrm{d}c^\beta}{\delta I(\boldsymbol{r}_1)}. \tag{C6}$$

The second derivative of equation (C5) is more complicated; for the particular case $I = J$, it is:

$$\begin{aligned} 0 = {} & \frac{\mathrm{d}^2 c^\beta}{\delta I(\boldsymbol{r}_1) \delta I(\boldsymbol{r}_2)} (\langle J_{\alpha\beta}, I - J \rangle - \langle J_\beta, J_\alpha \rangle) \\ & - \frac{\mathrm{d}c^\beta}{\delta I(\boldsymbol{r}_1)} \frac{\mathrm{d}c^\gamma}{\delta I(\boldsymbol{r}_2)} (\langle J_{\alpha\beta}, J_\gamma \rangle + \langle J_{\beta\gamma}, J_\alpha \rangle \\ & + \langle J_{\gamma\alpha}, J_\beta \rangle - \langle J_{\alpha\beta\gamma}, I - J \rangle) \\ & + \frac{\mathrm{d}c^\beta}{\delta I(\boldsymbol{r}_1)} J_{\alpha\beta}(\boldsymbol{r}_2) + \frac{\mathrm{d}c^\beta}{\delta I(\boldsymbol{r}_2)} J_{\alpha\beta}(\boldsymbol{r}_1). \end{aligned} \tag{C7}$$

Defining $\mathbf{H}$ to be the matrix inverse of $[\mathbf{H}^{-1}]_{\alpha\beta} = \langle J_\alpha, J_\beta \rangle$, and evaluating the derivatives at $I = J$, gives

$$\left. \frac{\mathrm{d}c^\beta}{\delta I(\boldsymbol{r})} \right|_{I=J} = H^{\alpha\beta} J_\alpha(\boldsymbol{r}) \tag{C8}$$

and

$$\int \left. \frac{\mathrm{d}^2 c^\beta}{\delta I(\boldsymbol{r}) \delta I(\boldsymbol{r})} \right|_{I=J} \mathrm{d}^2\boldsymbol{r} = -H^{\alpha\beta} H^{\gamma\delta} \langle J_\alpha, J_{\gamma\delta} \rangle. \tag{C9}$$

In equation (C9) we have only computed the trace of the second derivative matrix; this is all we will need.

A circular Gaussian galaxy with unit radius and central intensity has measured profile:

$$\hat{I}(\boldsymbol{r}) = \mathrm{e}^{-(x^2+y^2)/2} + \eta(\boldsymbol{r}) = J(\boldsymbol{r}; C^\alpha) + \eta(\boldsymbol{r}), \tag{C10}$$

where η is the noise and $C^\alpha = (1, 0, 0, 1, 0, 1)$ are the moments of the galaxy (in the absence of noise). The noise is assumed to be white:

$$\langle \eta(\boldsymbol{r}_1) \eta(\boldsymbol{r}_2) \rangle = \mathcal{N} \delta^{(2)}(\boldsymbol{r}_1 - \boldsymbol{r}_2). \tag{C11}$$

The mean and covariance of the measured moments $\hat{c}^\alpha$ can then be determined to order $O(\mathcal{N})$ from the equations:

$$\langle \hat{c}^\alpha \rangle = C^\alpha + \frac{1}{2} \mathcal{N} \int \left. \frac{\mathrm{d}^2 c^\alpha}{\delta I(\boldsymbol{r}) \delta I(\boldsymbol{r})} \right|_{I=J} \mathrm{d}^2\boldsymbol{r} \tag{C12}$$

and

$$\mathrm{Cov}(\hat{c}^\alpha, \hat{c}^\beta) = \mathcal{N} \int \left. \frac{\mathrm{d}c^\alpha}{I(\boldsymbol{r})} \frac{\mathrm{d}c^\beta}{I(\boldsymbol{r})} \right|_{I=J} \mathrm{d}^2\boldsymbol{r}. \tag{C13}$$

Substituting equations (C8) and (C9) yields:

$$\langle \hat{c}^\alpha \rangle = C^\alpha - \frac{1}{2} \mathcal{N} H^{\alpha\beta} H^{\gamma\delta} \int J_\beta(\boldsymbol{r}) J_{\gamma\delta}(\boldsymbol{r}) \, \mathrm{d}^2\boldsymbol{r} \tag{C14}$$

and

$$\mathrm{Cov}(\hat{c}^\alpha, \hat{c}^\beta) = \mathcal{N} H^{\alpha\beta}. \tag{C15}$$

The substitution of the particular functional form equation (C2) into equations (C14) and (C15) is a straightforward but lengthy exercise. The $\mathbf{H}$ matrix in the basis of equation (C1) is

$$\mathbf{H} = \frac{2}{\pi} \begin{pmatrix} 1 & 0 & 0 & 1 & 0 & 1 \\ 0 & 1 & 0 & 0 & 0 & 0 \\ 0 & 0 & 1 & 0 & 0 & 0 \\ 1 & 0 & 0 & 4 & 0 & 0 \\ 0 & 0 & 0 & 0 & 2 & 0 \\ 1 & 0 & 0 & 0 & 0 & 4 \end{pmatrix} \tag{C16}$$

and the product $H^{\gamma\delta} J_{\gamma\delta}(\boldsymbol{r})$ appearing in equation (C14) is

$$H^{\gamma\delta} J_{\gamma\delta}(\boldsymbol{r}) = \frac{2}{\pi} (\rho^4 - 2) \mathrm{e}^{-\rho^2/2}. \tag{C17}$$

From this we find that the mean values of the entries in $\mathbf{M}^{-1}$ are

$$\langle[\hat{M}^{-1}]^{xx}\rangle = \langle[\hat{M}^{-1}]^{yy}\rangle = 1 + \frac{8}{\pi}\mathcal{N} \tag{C18}$$

and $\langle[\hat{M}^{-1}]^{xy}\rangle = 0$. Using the Taylor series for the moments:

$$\hat{\mathbf{M}} = \mathbf{1} - (\hat{\mathbf{M}}^{-1} - \mathbf{1}) + (\hat{\mathbf{M}}^{-1} - \mathbf{1})^2 + O(\hat{\mathbf{M}}^{-1} - \mathbf{1})^3, \tag{C19}$$

we can find the mean of $\hat{\mathbf{M}}$ to be

$$\langle\hat{M}_{ij}\rangle = \left(1 + \frac{4}{\pi}\mathcal{N}\right)\delta_{ij} \tag{C20}$$

and the covariance to be:

$$\mathrm{Cov}(\hat{M}_{ij}, \hat{M}_{kl}) = \frac{4}{\pi}\mathcal{N}(\delta_{ik}\delta_{jl} + \delta_{il}\delta_{jk}). \tag{C21}$$

We now generalize equations (C20) and (C21). Clearly, the energy functional is translation-invariant, so equations (C20, C21) cannot depend on $\boldsymbol{r}_0$. If the amplitude A is increased by some factor, and the noise amplitude $\sqrt{\mathcal{N}}$ is similarly increased, the energy minimization remains unchanged, so the result can depend on A and $\mathcal{N}$ only through the ratio $A/\sqrt{\mathcal{N}}$. The problem is also invariant under linear transformations of $\boldsymbol{r}$, so that if $\mathbf{M}$ is changed, and $\mathcal{N}$ is increased by the factor $\sqrt{\det\mathbf{M}}$ [to account for the delta function in equation (C11) and the change of measure in the integration over $\mathrm{d}^2\,\boldsymbol{r}$], then the linear transformation acts simply on equations (C20, C21). We have concluded that the generalizations of equations (C20, C21) are

$$\langle\hat{M}_{ij}\rangle = \left(1 + 4\frac{\mathcal{N}}{\pi A^2\sqrt{\det\mathbf{M}}}\right)M_{ij} \tag{C22}$$

and

$$\mathrm{Cov}(\hat{M}_{ij}, \hat{M}_{kl}) = 4\frac{\mathcal{N}}{\pi A^2\sqrt{\det\mathbf{M}}}(M_{ik}M_{jl} + M_{il}M_{jk}). \tag{C23}$$

The quantity $\mathcal{N}/\pi A^2\sqrt{\det\mathbf{M}}$ is recognized as ν^{-2}, where ν is the signal-to-noise ratio for detection of the galaxy in an adaptive elliptical Gaussian filter (Bernstein & Jarvis 2002).

We have reached the final stage in our plan, namely to translate the errors in $\mathbf{M}$ into the calibration bias of the ellipticity estimator. We consider here only the simplest case, that of a circular Gaussian PSF and an elliptical Gaussian galaxy with its major axis aligned along the x-axis. The estimated ellipticity is:

$$\hat{e}_+^{(f)} = \frac{\hat{Q}^{(I)}}{\hat{T}^{(I)} - T^{(P)}}, \tag{C24}$$

where T is the trace and $Q = M_{xx} - M_{yy}$ is the + quadrupole moment. The effects of the bias (equation C22) and noise (equation C23) in $\mathbf{M}^{(I)}$ can be determined from the first and second derivatives (respectively) of $\hat{e}_+^{(f)}$ with respect to $\mathbf{M}^{(I)}$; the order $O(\mathcal{N})$ terms are:

$$\begin{aligned}\left\langle\hat{e}_+^{(f)}\right\rangle = e_+^{(f)} &+ \frac{\left\langle\delta\hat{Q}^{(I)}\right\rangle}{T^{(I)} - T^{(P)}} - \frac{Q^{(I)}\left\langle\delta\hat{T}^{(I)}\right\rangle}{\left[T^{(I)} - T^{(P)}\right]^2} \\ &- \frac{\mathrm{Cov}\left[\hat{Q}^{(I)}, \hat{T}^{(I)}\right]}{\left[T^{(I)} - T^{(P)}\right]^2} + \frac{Q^{(I)}\left\langle\left[\delta\hat{T}^{(I)}\right]^2\right\rangle}{\left[T^{(I)} - T^{(P)}\right]^3},\end{aligned} \tag{C25}$$

where we have used the bias $\langle\delta\hat{Q}\rangle = \langle\hat{Q}\rangle - Q$. For a galaxy with only + ellipticity (i.e. position angle along the x- or y-axis), the biases and covariances obtained from equations (C22, C23) are:

$$\begin{aligned}&\left\langle\delta\hat{Q}^{(I)}\right\rangle = 4\nu^{-2}T^{(I)}e_+^{(I)}; \\ &\left\langle\delta\hat{T}^{(I)}\right\rangle = 4\nu^{-2}T^{(I)}; \\ &\left\langle\left[\delta\hat{T}^{(I)}\right]^2\right\rangle = 4\nu^{-2}T^{(I)2}\left[1 + e_+^{(I)2}\right]; \\ &\mathrm{Cov}\left[\hat{Q}^{(I)}, \hat{T}^{(I)}\right] = 8\nu^{-2}T^{(I)2}e_+^{(I)}; \\ &\left\langle\left[\delta\hat{Q}^{(I)}\right]^2\right\rangle = 4\nu^{-2}T^{(I)2}\left[1 + e_+^{(I)2}\right].\end{aligned} \tag{C26}$$

This leads us to the result for the change in ellipticity calibration:

$$\frac{\left\langle\delta\hat{e}_+^{(f)}\right\rangle}{e_+^{(f)}} = \frac{4}{\nu^2}\left[1 - 3R_2^{-1} + R_2^{-2} + e_+^{(f)2}\right]. \tag{C27}$$

We have verified equations (C22), (C23) and (C27) in ‘toy’ simulations.

We have used this result as an approximation to the shear calibration $\delta\gamma/\gamma$, although this is not exact because the shear calibration is determined by the derivative of $\langle\delta\hat{e}_+^{(f)}\rangle$ with respect to $e_+^{(f)}$, which is not exactly equal to the ratio $\langle\delta\hat{e}_+^{(f)}\rangle/e_+^{(f)}$ when the latter is not constant. The calibration bias obtained from equation (C27) is shown in Fig. 6.

APPENDIX D: CHI-SQUARED TEST WITH ERRORS FROM SIMULATIONS

We perform several tests for consistency with zero signal using a χ^2 test. Since we have derived our covariance matrix from simulations, we must also take into account the noise from only having a finite number of simulations.

If we have estimated a shear in N radial bins, we can construct an N-dimensional shear vector $\boldsymbol{\gamma}$. The M simulations provide us with M simulated shear vectors $\{\boldsymbol{\gamma}^{(\alpha)}\}_{\alpha=1}^{M}$ from which we can compute the sample covariance $\hat{\mathbf{C}}$ (see equation 33). We are interested in the distribution of the variable

$$\hat{\chi}^2 = \boldsymbol{\gamma}^T\hat{\mathbf{C}}^{-1}\boldsymbol{\gamma} \tag{D1}$$

under the null hypothesis that $\boldsymbol{\gamma}$ is Gaussian with mean $\mathbf{0}$ and the same covariance $\mathbf{C}$ as the simulated shear vectors.

In order to determine the distribution of $\hat{\chi}^2$ via Monte Carlo, we define the vectors $\boldsymbol{x} = \mathbf{C}^{-1/2}\,\boldsymbol{\gamma}$ and $\boldsymbol{x}^{(\alpha)} = \mathbf{C}^{-1/2}\,\boldsymbol{\gamma}^{(\alpha)}$. (Here the symmetric matrix $\mathbf{C}^{-1/2}$ has the same eigenvectors as $\mathbf{C}$ but the eigenvalues λ_i are replaced by $\lambda_i^{-1/2}$.) Then we find:

$$\hat{\chi}^2 = \boldsymbol{x}^T\mathbf{D}^{-1}\boldsymbol{x}, \tag{D2}$$

where the matrix $\mathbf{D}$ is given by:

$$\mathbf{D} = \frac{1}{M-1}\left[\sum_{\alpha=1}^{M}\boldsymbol{x}^{(\alpha)}\boldsymbol{x}^{(\alpha)T} - \bar{\boldsymbol{x}}\bar{\boldsymbol{x}}^T\right], \tag{D3}$$

where $\bar{\boldsymbol{x}}$ are the sample means of the $\boldsymbol{x}^{(\alpha)}$. Since the x_i and $x_i^{(\alpha)}$ are independent Gaussians of zero mean and unit variance, it is computationally easy to generate sample from equation (D3), so we can use a Monte Carlo method to compute the probability distribution for $\hat{\chi}^2$.

As $M \to \infty$ (with fixed N), $\mathbf{D} \to \mathbf{1}$ and the distribution of $\hat{\chi}^2$ converges to the χ^2 distribution. However, the convergence is not rapid. To see this, we note that by Wick’s theorem, $\mathbf{D}$ has expectation value equal to the identity $\mathbf{1}$ and covariance:

$$\langle(D_{ij} - \delta_{ij})(D_{kl} - \delta_{kl})\rangle = \frac{\delta_{ik}\delta_{jl} + \delta_{il}\delta_{jk}}{M-1}. \tag{D4}$$

Using the Taylor series for the inverse of a matrix, and the fact that the higher-order moments of the **D** distribution decrease as M^{-2} or faster, we find the asymptotic expansion:

$$\langle \mathbf{D}^{-1} \rangle = \mathbf{1} + \langle (\mathbf{D} - \mathbf{1})^2 \rangle + O(M^{-2}). \tag{D5}$$

Since $\boldsymbol{x}$ is independent of **D**:

$$\langle \hat{\chi}^2 \rangle = N + \frac{N(N+1)}{M} + O(M^{-2}), \tag{D6}$$

which is found to agree with the mean obtained via Monte Carlo. Since the standard deviation of the χ^2 distribution is $\sqrt{2N}$, we must take $M \gg N^{3/2}$ in order for the $O(1/M)$ correction term in equation (D6) to be small compared with the width of the χ^2 distribution. Therefore, the standard χ^2 test is only valid if $M \gg N^{3/2}$ (not true for our random lens test, with $M = 78$ and $N = 39$).

This paper has been typeset from a TEX/LATEX file prepared by the author.